POLITECNICO DI TORINO

Master Degree in Electronic Engineering



Politecnico di Torino

Development of a MOPA fiber laser architecture for emission around 2 µm: simulation and experimental implementation

Supervisor:
Prof. Guido Perrone

Candidate:
Federico Cobianchi

Co-Supervisor:
Dott. Chiara Bellezza Prinsi
Dott. Valentina Serafini

A.A 2025/2026

E quindi uscimmo a riveder le stelle.

Dante

Abstract

Thulium-doped fiber lasers (TDFLs) operating around 1.9 µm to 2 µm are increasingly employed in surgical applications such as soft-tissue ablation, lithotripsy and hemostasis thanks to the strong water absorption and eye-safe nature of this spectral window. Achieving the high output power required for these procedures typically relies on a Master Oscillator Power Amplifier (MOPA) architecture in which a Thulium-Doped Fiber Amplifier (TDFA) boosts a seed signal while preserving beam quality and stable operation. Reliable design of such amplifiers requires accurate simulation tools capable of predicting gain, power scaling and thermal behavior under realistic operating constraints including strict limits on laser diode and driver temperature (below 40 °C in this work).

This thesis addresses the design, simulation and characterization of a high-power TDFA targeting 10 W output power at approximately 1940 nm. A numerical model based on the rate and propagation equations was developed in MATLAB and cross-validated against simulations performed in RP Fiber Power allowing the evaluation of in-band pumping schemes and fiber length optimization within the MOPA chain. Thermal management was addressed through a fully passive cooling scheme: the pump laser diode and driver electronics were shown to remain below the 40 °C safety limit under worst-case operating conditions with a measured temperature rise of only a few degrees above ambient. On the optical side, the onset of Stimulated Brillouin Scattering (SBS) was identified as the main limiting factor for short-pulse operation, setting a minimum achievable pulse duration of 0.2 ms for the amplifier configuration under study.

The validity of this thesis work was assessed by comparing the simulation results against experimental measurements carried out in the laboratory using available rare-earth-doped fibers such as Er- and Yb/Er-doped fibers. The close agreement observed between the simulated and experimental data confirms the accuracy of the proposed model in reproducing both the thermal and optical behavior of the system thereby validating the overall simulation approach.

Overall, this work demonstrates that starting from a low power seed it is possibile to achieve a watt-level design capable of delivering several different pulses ranging from hundreds of microseconds to hundreds of milliseconds. The developed system represents a good working principle for a laser system capable to work in a surgical environment and able to address some of the problems related to the common way to treating a patient.

Table of Contents

Abstract **I**

List of Figures **VI**

List of Tables **VII**

Acronyms **IX**

1 Introduction **1**
1.1 Motivation and context 1
1.2 Scope of the work 2
1.3 Outline of the thesis 2

2 Overview on laser Technology **5**
2.1 Historical background 5
2.2 What is a laser 6
2.3 Light amplification 11
2.4 MOPA laser 14
2.5 Applications of lasers 15

3 Thermal management **19**
3.1 Simulation software and theoretical background 20
3.2 Heatsink vs generic plate 22
3.3 Fiber heat spreading 23
3.4 Fiber laser simulation 24
3.5 Final simulation 25
3.6 Experimental results 27
3.6.1 Thermal response under active and passive cooling 27
3.6.2 Dynamic thermal behavior 29

4 TDFA simulations **33**
4.1 Physical quantities relevant to laser-tissue interaction 34
4.2 Theoretical principles and equations behind the simulation 36
4.3 RP simulations 38
4.3.1 Optical simulations 38
4.3.2 Stimulated Brillouin Scattering 43
4.3.3 Simulated physical quantities for laser-tissue interaction and comparison with reference values 45
4.4 MATLAB simulations 46
4.4.1 Optical simulations 46

4.5 Comparison of the results of the two simulations 48

5 Experimental evaluation **53**
5.1 Experimental setup 53
5.1.1 Theory 54
5.2 Experimental setup characterization 55
5.2.1 Simulation vs. experimental measurements 56
5.2.2 Physical quantities relevant to laser-tissue interaction, comparison between: theory, simulation and experimental evaluation 58
5.2.3 Effect of pump power on signal characteristics 58

6 Conclusion **63**

Bibliography **68**

List of Figures

1.1 Water absorption spectrum [1]. 2

2.1 Oscillator model. 8
2.2 Active region cross-section seen across the propagation direction. . . 8
2.3 FP resonator (left) and DFB resonator (right). 9
2.4 Butterfly package [2] (left) and Internal structure of the butterfly package [3] (right). 10
2.5 Typical P-I characteristic curve of a DFB laser (left) and dependence of the wavelength from the temperature (right). The graphs are provided for illustrative purposes only as 1550 nm is a telecommunication wavelength rather than a biomedical one. 10
2.6 Optical signal amplification through stimulated emission, $h\nu$ represents an incoming/generated photon. 11
2.7 Diagram of Thulium energy levels, dashed line between E_3 and E_2 represents a non-radiative decay (heat). 12
2.8 Different types of double cladding fiber, the different inner cladding shapes allow a different superposition of the pump modes on the core [4]. 13
2.9 Setup for a single stage MOPA. 15
2.10 Power needed by different industrial application and which type of laser can be used to generate said power [5]. 16
2.11 Skin depth penetration of 1000 nm (Ytterbium) and 2000 nm (Thulium) laser, image taken from [6]. 17

3.1 3D model (left) and Thermal simulation (right) of heat dissipation through Copper plate. 23
3.2 3D model (left) and Thermal simulation (right) of heat dissipation through Copper Heatsink. 23
3.3 3D model (left) and Thermal simulation (right) of heat generated by the active fiber. 24
3.4 3D model (left) and Thermal simulation (right) of the laser and active fiber positioned on top of an Aluminum plate. 25
3.5 3D model (left) and Thermal simulation (right) of the complete system with the proper Computer-Aided Design (CAD) models and materials. 27
3.6 Thermal simulation of the complete system with the proper CAD models and materials dissipated by an active cooling device. 27
3.7 Temperature reached by the laser diode and the driver module with a passive cooling system capture with a thermal camera, Sp1 corresponds to the laser diode and spot Sp2 corresponds to the driver. . 29

3.8 Temperature reached by the laser diode and the driver module with an active cooling system capture with a thermal camera, Sp1 corresponds to the driver and spot Sp2 corresponds to the laser diode. . 29
3.9 Thermal behavior of the pump laser diode and driver electronics under active (a) and passive (b) cooling. 30
3.10 Comparison between the simulated and experimental heating and cooling temperature transient for the passive cooling system. 31

4.1 Diagram of the simplified Thulium energy levels, τ is the average lifetime of the electrons laying in the excited state. 36
4.2 Evolution of the signal amplification and pump absorption as a function of the fiber length. 39
4.3 Correlation between input pump power and output signal power. . . 40
4.4 ASE spectrum between 1350 nm and 2100 nm [7]. 40
4.5 Amplification of a single pulse with different pulse durations and repetition rate. 41
4.6 Pulse train for soft tissue ablation. 42
4.7 Pulse train for kidney stone ablation. 42
4.8 Pulse train for hemostasis. 43
4.9 The traveling lightwave has both electrical field (E) and magnetic field (B) components (left), the lightwave (photons) interact with the vibrational states of the material (phonons) changing the photons energy and consequently their wavelength (right) [8]. 44
4.10 Example of SBS induced damages [4]. 45
4.11 Pulse train for soft tissue ablation. 47
4.12 Pulse train for kidney stone ablation. 47
4.13 Pulse train for hemostasis. 48
4.14 Comparison between different pulse trains for soft tissue ablation. . 50
4.15 Comparison between different pulse trains for kidney stone ablation. 50
4.16 Comparison between different pulse trains for hemostasis. 51

5.1 Experimental setup implemented MOPA laser. 54
5.2 Diagram of co-doped Erbium/Ytterbium energy levels [9]. 55
5.3 Comparison between MATLAB and RP Fiber Power simulation with experimental data. 56
5.4 Comparison between MATLAB and RP Fiber Power simulation with experimental data. 57
5.5 Comparison between MATLAB and RP Fiber Power simulation with experimental data. 57
5.6 Superposition of pulses used for ablation of soft tissues at different pump power, pulse duration = 10 ms and repetition rate = 20 Hz. . 60
5.7 Superposition of pulses used for ablation of kidney stones at different pump power, pulse duration = 0.2 ms and repetition rate = 500 Hz. 60
5.8 Superposition of pulses train used for hemostasis at different pump power, pulse duration = 200 ms and repetition rate = 1 Hz. 61

List of Tables

3.1 Thermophysical properties of the materials used in the simulations . 20
3.2 Volume, total power, and power density of the heat-generating components 20
3.3 Components and materials of the simulated devices 25
3.4 Volume, total power, and power density of the heat-generating components 26

4.1 laser's parameters for Ablation and Hemostasis 34
4.2 Pulse's energy for Ablation and Hemostasis, [10–13] 35
4.3 Parameters of the simulation 39
4.4 Simulated pulses 43
4.5 Pulse's energy for Ablation and Hemostasis, [10–13] 46

5.1 Pulse's energy for Ablation and Hemostasis. Comparison of the different values: theory, simulation and experimental evaluation 58

Acronyms

ASE Amplified Spontaneous Emission. 11, 14, 35, 38

CAD Computer-Aided Design. 19, 23–25, 61

CW Continuous Wave. 5, 9, 32

DFB Distributed Feedback. 6, 8, 9

DWDM Dense Wavelength Division Multiplexing. 9

EDFA Erbium-Doped Fiber Amplifier. 6

FEM Finite Element Modelling. 19

FP Fabry-Pérot. 8, 9

GaAs Gallium Arsenide. 5, 8

GUI Graphic User Interface. 19

InP Indium Phosphide. 8

LIDAR Light Detection and Ranging. 14

MASER Microwave Amplification by Stimulated Emission of Radiation. 5, 42

MBE Molecular Beam Epitaxy. 6

MOCVD Metal-Organic Chemical Vapor Deposition. 6

MOPA Master Oscillator Power Amplifier. 2, 13, 14, 33, 51, 52, 61, I

Nd:YAG Neodymium-doped Yttrium Aluminum Garnet. 7

OSNR Optical Signal-to-Noise Ratio. 11

SBS Stimulated Brillouin Scattering. 14, 31, 38, 39, 41–43, I

SBST SBS Threshold power. 42, 43

SMSR Side-Mode Suppression Ratio. 8

SRS Stimulated Raman Scattering. 14

TDFA Thulium-Doped Fiber Amplifier. 2, 3, 6, 10, 11, 13, 22, 31, 51, 57, I

TDFL Thulium-doped fiber laser. I

TEC ThermoElectric Coolers. 9

TIM Thermal Interface Material. 20, 22–24

Chapter 1

Introduction

1.1 Motivation and context

The history of medicine is full of examples of surgical interventions aimed at improving patients' living conditions or treating a pathology they suffer from. Over time, especially in the last century, surgical techniques have been substantially modified and improved in order to address the two main drawbacks of classical surgery: the inherent risk of the operation itself and the recovery time required of the patient. In some cases, such as elderly patients or particularly invasive procedures, recovery may not be complete. For this reason, medicine has been increasingly shifting towards minimally invasive techniques capable of completing the operation while causing as little damage as possible. Due to the rise in the number of minimally invasive surgeries there has been a great deal of interest in medical lasers capable of delivering a controlled amount of optical power into biological tissues. An accurate and targeted control over cutting, ablating or coagulating biological tissue within a very small region of collateral damage is a fundamental requirement for various clinical applications, from urology to neurosurgery. In this context, the operating wavelength plays a critical role, as it determines both the depth to which radiation penetrates into tissue and how effectively it is converted into the thermal energy required to produce a clinical effect. The region around 2 µm is particularly interesting due to the high absorption of water molecules in this range. Fig. 1.1 shows how the absorption coefficient varies with wavelength. Predominantly water-based biological tissues absorb light strongly at this wavelength, leading to a small penetration depth of about 300 µm, thus localising the thermal effect within a defined volume around the treatment site and reducing thermal damage to healthy tissue.

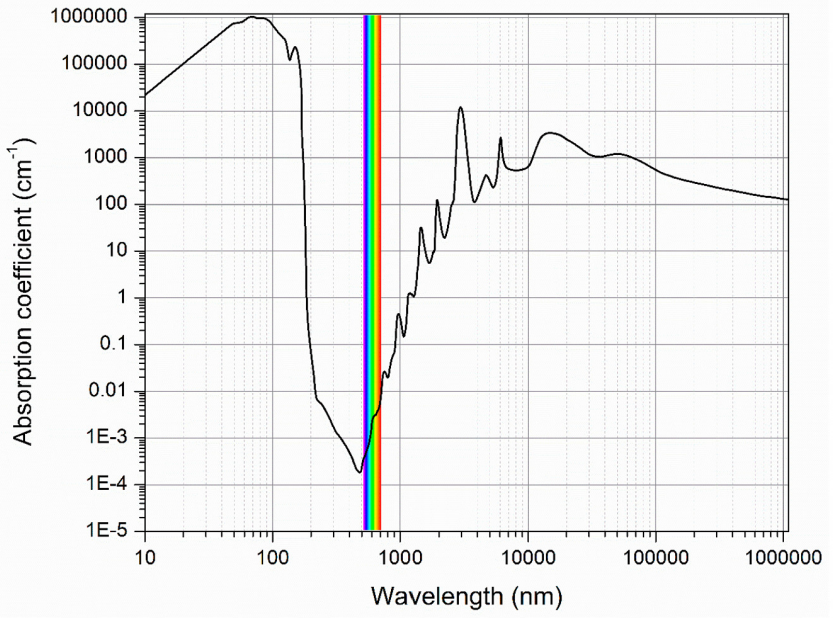


Figure 1.1: Water absorption spectrum [1].

1.2 Scope of the work

This thesis has the following goals:

1. Simulate the laser both thermally and optically, comparing the results to experimental values to assess whether the models are capable of modelling the real case scenario and can, therefore, be used for further simulations.

2. Build a Thulium laser capable of delivering 10 W, either continuously or in pulsed mode.

3. Use only a passive cooling solution in order to be able to use the laser in surgical rooms.

Motivated by these goals, this thesis presents the characterization and investigation of a MOPA laser system utilizing a TDFA operating around the emission wavelength of 1940 nm. A stable, narrowband output from a low-power seed laser is amplified to the required power level through the amplifier stage. The system is configured to deliver a nominal output power of 10 W and is designed to operate either continuously or, more importantly, in pulsed mode. The ability to operate in pulsed mode is critical for potential surgical applications such as soft tissue ablation, kidney stone fragmentation and hemostasis.

1.3 Outline of the thesis

The thesis is structured as follows. In chapter 2 the laser technology has been summarized by introducing basic concepts concerning working mechanisms, MOPA system and biomedical application that made desirable using Thulium as active

medium. In chapter 3 there have been shown results of simulations about the passive cooling system of the system. In chapter 4 have been showed simulation results related to TDFA optical stage using RP Fiber Power and a personal implementation in MATLAB. Lastly, chapter 5 is dedicated to the experimental evaluation and the comparison between the simulation and what was measured during the laboratory session.

Chapter 2

Overview on laser Technology

2.1 Historical background

The theoretical foundations of laser technology trace back to the early twentieth century. In 1917 Einstein introduced the concept of stimulated emission, establishing the physical principle upon which all laser operation is based. However, translating this idea into a working device required several more decades of theoretical and experimental development.

The first milestone was reached in 1954 when the first Microwave Amplification by Stimulated Emission of Radiation (MASER) was demonstrated. That device was used to amplify microwave radiation through stimulated emission in ammonia molecules [14]. This work created the basis for experimental coherent radiation amplification and laid the conceptual groundwork for extending the principle to other frequency ranges. The theoretical extension of the maser concept to the optical domain and, most importantly, to the infrared part of the spectrum was proposed in 1958 [15]. This paper described the conditions under which population inversion and optical feedback could be achieved in a resonant cavity providing the starting point for what would become the laser. The first working laser was demonstrated in 1960 by Theodore Maiman who achieved stimulated optical emission in a synthetic ruby crystal pumped by a pulsed flashlamp. Shortly after, thanks to this result, the scientific community began exploring alternative gain media. In 1961 was demonstrated the first gas laser (helium-neon mixture) which produced Continuous Wave (CW) coherent emission in the infrared [16]. This achievement was significant because it demonstrated that laser operation was not restricted to only solid-state media thus opening the door to a much broader range of laser architectures. The development of semiconductor lasers began in earnest in 1962 when multiple research groups simultaneously and independently demonstrated coherent light emission from Gallium Arsenide (GaAs) p-n junctions under forward bias. Among these stimulated emission from GaAs at cryogenic temperatures under pulsed electrical excitation was achieved [17]. These early devices however suffered from extremely high threshold current and could only operate under pulsed conditions at liquid nitrogen temperatures. Due to this problem their practical applicability remained extremely limited.

The breakthrough that enabled room-temperature continuous-wave operation of semiconductor lasers came with the introduction of the double-heterostructure con-

cept in the late 1960s. The usage of heterojunction structures to achieve carrier and optical confinement simultaneously was proposed in [18] while experimental realization of double-heterostructure lasers were carried out and demonstrated the superior performance compared to homojunction devices [19]. By confining both the injected carriers and the optical mode within a thin active layer putted between cladding layers these structures dramatically reduced the threshold current. The practical consequences of this development were enormous as semiconductor lasers could now operate continuously at room temperature making them usable for real-world deployment. Throughout the 1970s and 1980s advances in epitaxial growth techniques, particularly in Molecular Beam Epitaxy (MBE) and Metal-Organic Chemical Vapor Deposition (MOCVD), allowed for increasingly precise control over the composition and thickness of semiconductor layers. This in turn enabled the fabrication of quantum well lasers in which the active region is reduced to a thickness of only a few nanometers resulting in a discrete density of states and further reduced threshold currents and improved the efficiency. The development of single frequency lasers sources became a priority as optical fiber communications emerged as a dominant technology. Distributed Feedback (DFB) lasers, in which a Bragg grating is integrated directly into the laser cavity to provide wavelength-selective feedback, were proposed and demonstrated during this period. These devices offered the narrow spectral linewidth and mode stability required for high-capacity optical transmission systems. Thanks to their reliability and their clean output spectra they still are the dominant source in fiber-optic communications to this day. Parallel to these developments in semiconductor lasers, significant progress were made in fiber based laser and amplifier technology. In 1987 was demonstrated an high-gain optical amplification in an erbium-doped single-mode fiber at 1.53 µm [20]. This result proved that an all-optical signal amplification without any electrical conversion can be created and allowed long distance optical communication to take place without an optic-eletric conversion/amplification. The success of the Erbium-Doped Fiber Amplifier (EDFA) in the 1550 nm telecommunication window stimulated broad interest in other rare-earth-doped fiber systems including TDFAs which operate in the 1900 nm-2000 nm region. TDFAs are particularly relevant to the work described in this thesis. The maturation of high-power fiber laser technology over the subsequent decades, driven by advances in double-clad fiber design and high-brightness pump diode lasers, enabled output powers scaling from milliwatts to kilowatts while maintaining excellent beam quality [21]. This progress, combined with the availability of reliable single-frequency seed sources and low-noise amplifier stages, made the Master Oscillator Power Amplifier architecture increasingly attractive for both scientific and industrial applications. Today laser technology spans an extraordinary range of wavelengths, pulse durations and output powers forming the foundation for applications in telecommunications, manufacturing, medicine and fundamental research.

2.2 What is a laser

A laser is an optical device that generates a coherent and monochromatic beam of light. Its fundamental working principle relies on an active gain medium (active region), where an external energy source creates a state of population inver-

sion. Depending on the application the gain medium can take very different forms such as a semiconductor p-n junction, a doped fiber or a solid-state crystal like Neodymium-doped Yttrium Aluminum Garnet (Nd:YAG). In semiconductor lasers, or laser diodes, the population inversion is reached by means of current injection into the active region. The dynamics of the carrier population and photon density inside the active region are described by a set of equations called "rate equations". Although the general framework of rate equations can be applied to different types of lasers the formulation presented in this thesis refers specifically to the semiconductor laser case:

$$\begin{aligned} \frac{dN}{dt} &= \frac{\eta_i I}{qV} - \frac{N}{\tau} - v_g g N_p \\ \frac{dN_p}{dt} &= \Gamma v_g g N_p + \Gamma \beta_{sp} R_{sp} - \frac{N_p}{\tau_p} \end{aligned} \tag{2.1}$$

Where N represents the carrier density, N_p the photon density, I the current used to achieve population inversion, V the active region volume, τ the carrier lifetime, τ_p the photon lifetime, v_g the group velocity and g the gain. If we put the gain medium inside an optical resonator (or cavity) the system is provided of an optical feedback and light starts to bounce back and forth between the cavity mirrors. This feedback is typically achieved using partially reflecting mirrors at both ends of the cavity. For sustained laser oscillation to occur, the system must satisfy the Barkhausen conditions. The amplitude condition dictates that the round-trip gain must be large enough to exactly compensate for all internal losses and mirror leakage:

$$\Gamma g = \frac{1}{L_a} \ln\left(\frac{1}{R_1 R_2}\right) + \alpha_i = \alpha_m + \alpha_i \tag{2.2}$$

Where α_m is the mirror loss and α_i is the intrinsic loss of the cavity. At the same time the phase condition requires that the overall phase shift after a round trip must be an integer multiple of 2π to ensure constructive interference:

$$\lambda_m = \frac{2 n_{eff} L_a}{m} \tag{2.3}$$

Fig. 2.1 and Fig. 2.2 show the diagram used to model the oscillator and the the cross section of the laser's structure seen along the propagation direction. The "i" layer is the intrinsic semiconductor used as the gain medium, this is the region in which the population inversion occurs. Moreover, the two mirrors are drew as two rectangles called "R1" and "R2".

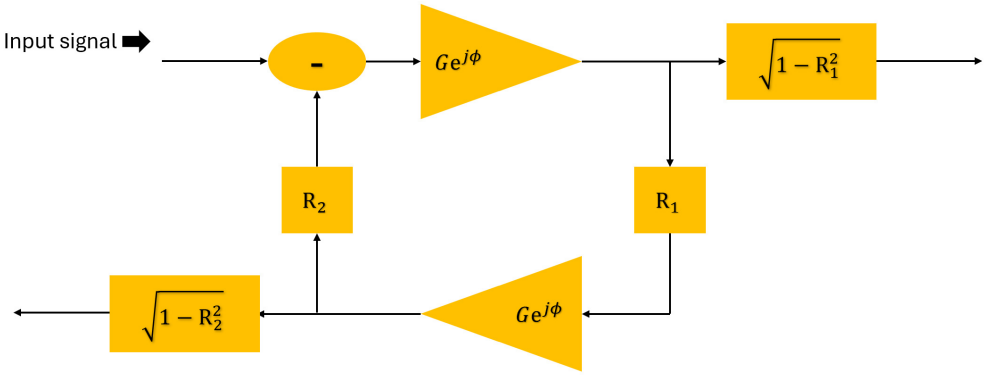


Figure 2.1: Oscillator model.

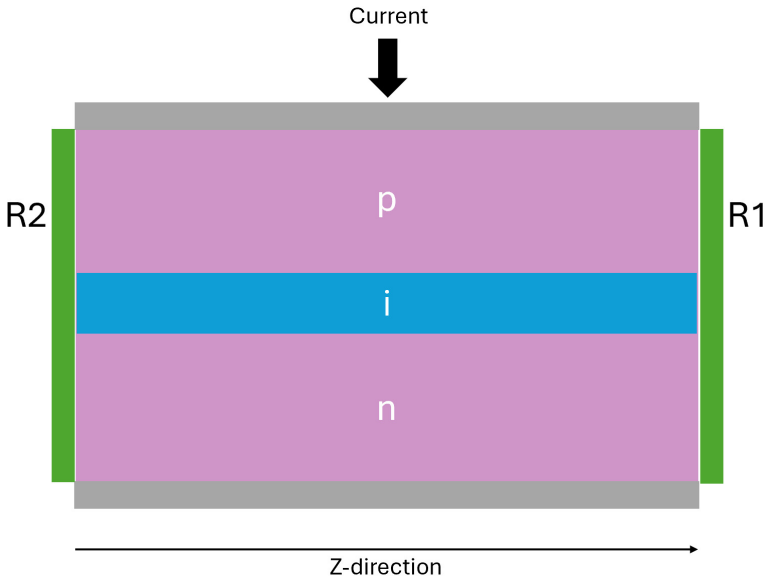
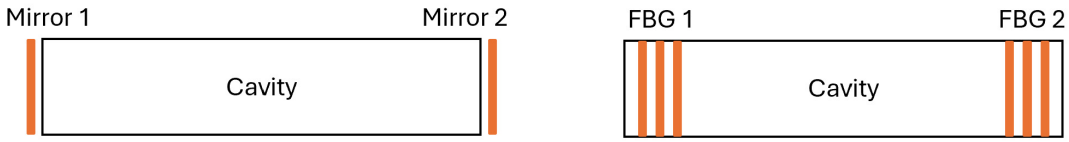


Figure 2.2: Active region cross-section seen across the propagation direction.

Among the many physical implementations that satisfy these conditions semiconductor lasers (also known as laser Diodes) stand out for their compactness, efficiency and compatibility with electronic driving circuitry making them the natural subject of this work. Moreover, they are used for their small size, high reliability and high electro-optic conversion efficiency [22]. Their fundamental working principle is based on stimulated emission within a solid-state gain medium (active region). Inside this region the injected carriers (electrons) will populate the conduction and valence band and then they'll recombine and generate coherent light. These devices are typically fabricated from III-V or II-VI compound materials [23] allowing for precise wavelength targeting based on the material's bandgap energy. Common material include Indium Phosphide (InP)-based compounds for telecom wavelengths around 1310 nm and 1550 nm and GaAs-based compounds for shorter wavelengths in the 780 nm-980 nm range. The emitted wavelength λ is primarily determined by the bandgap energy E_g of the active region material following the relation:

$$\lambda = \frac{hc}{E_g} \tag{2.4}$$

where h is Planck's constant and c is the speed of light in vacuum. In order to achieve lasing an optical feedback is required in addition to optical gain. In Fabry-Pérot (FP) laser diodes the optical feedback is provided by the cleaved facets of the semiconductor crystal which act as partially reflective mirrors due to the refractive index discontinuity at the semiconductor-air interface. However, FP lasers emit over multiple longitudinal modes resulting in a broad spectral linewidth that limits their use in high-end optical communication systems. For single-mode operation DFB lasers are employed. In this case a Bragg grating is incorporated directly into or adjacent to the active region along the laser cavity. This grating provides wavelength-selective feedback enabling single longitudinal mode emission with very narrow linewidths, typically on the order of a few MHz to a few hundred kHz, depending on the cavity design and operating conditions. The Side-Mode Suppression Ratio (SMSR) of DFB lasers typically exceeds 30 dB to 40 dB making them the preferred source for Dense Wavelength Division Multiplexing (DWDM) systems. Fig. 2.3 shows the difference between a FP cavity and a DFB cavity.



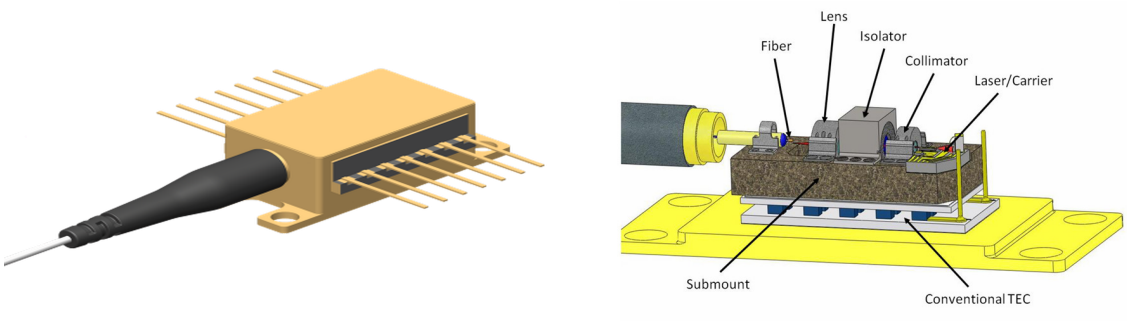
(a) (b)

Figure 2.3: FP resonator (left) and DFB resonator (right).

A major technical advantage of laser diodes is their capability for direct modulation up to several of gigahertz. It is worth noting that this property is relevant for signal laser diodes as high-power pump laser diodes are typically operated in CW mode and are not directly modulated. Their performance is highly sensitive to temperature and bias current fluctuations which can cause wavelength shifts and noise. The modulation bandwidth $f_{3\text{dB}}$ of a directly modulated laser is related to the relaxation oscillation frequency which in turn depends on the photon density inside the cavity and the differential gain of the active medium:

$$f_{3\text{dB}} = \frac{\sqrt{2}}{\tau_p}\left(1 + \frac{\Gamma \epsilon g_{th}}{a_0}\right)\frac{1}{2\pi} \tag{2.5}$$

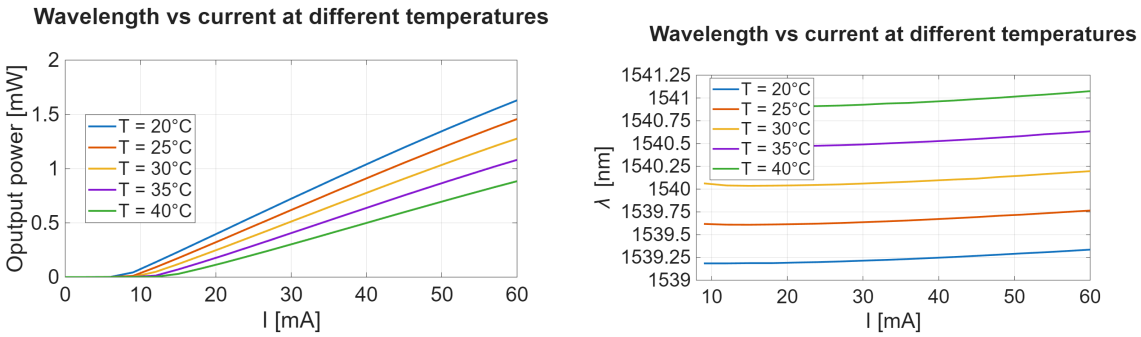
Temperature sensitivity is particularly critical in DFB laser, their emission wavelength shifts approximately 0.1 nm/°C. This is due to the temperature dependence of the refractive index. The threshold current increases exponentially with temperature leading to a lower efficiency whenever the laser's temperature increases too much. Consequently, commercial lasers are often housed in butterfly packages equipped with ThermoElectric Coolers (TEC) made of Peltier cells and monitor photodiodes to ensure stable operation. Fig. 2.4a shows what is a butterfly package while Fig. 2.4b shows the inside of said package. Both the laser chip and the TEC can be appreciated in the picture.



(a) (b)

Figure 2.4: Butterfly package [2] (left) and Internal structure of the butterfly package [3] (right).

A monitor photodiode, placed at the rear facet of the laser, provides a feedback signal proportional to the optical output power, enabling the driving circuitry to implement automatic power control loops that compensate for long-term aging and thermal drift. Regarding their emission capabilities the typical output optical power of these lasers ranges from a few milliwatts to, at best, 100 mW (0 dBm to 20 dBm). Depending on the specific design, commercial modules can achieve stable output levels of tens of mW up to 80 mW for high-end applications [24]. The relationship between injected current I and output optical power P is described by the P-I characteristic curve, which exhibits a well-defined threshold current I_{th} below which only spontaneous emission occurs. As said before the wavelength is also temperature dependent. The I_{th} vs Temperature can be seen in Fig. 2.5a while the wavelength vs temperature characteristic is displayed in Fig. 2.5b



(a) (b)

Figure 2.5: Typical P-I characteristic curve of a DFB laser (left) and dependence of the wavelength from the temperature (right). The graphs are provided for illustrative purposes only as 1550 nm is a telecommunication wavelength rather than a biomedical one.

2.3 Light amplification

As explained in the previous paragraph, signal laser diodes cannot emit power that exceeds 100 mW. Due to this fact it is necessary to amplify the laser's emitted light. In order to do so a device called "amplifier" is used. There are several different amplifier topologies, the one used in this thesis consists of a system made of a pump laser and a doped fiber, known as a TDFAs. This amplifier exploits the stimulated emission principle to amplify light without the need for any optical-to-electrical conversion. The stimulated emission principle, represented in Fig. 2.6, works as follows: thanks to the energy introduced into the fiber by the pump laser the Thulium ions (Tm^{3+}) that are part of the doped fiber get ionized, the atom goes from the ground state E_1 to a metastable excited state E_2. This process is called "population inversion". When a photon of the signal that must be amplified propagates near these electrons lying in the excited state stimulated emission takes place: the electron decays back to the ground state and emits a photon that is identical to the one that induced the transition sharing the same frequency, phase, polarization and direction of propagation. What was just described happens for all the electrons in the excited state E_2. Thank to this behavior we obtain amplification, the number of photon that exit the fiber is bigger than the input one.

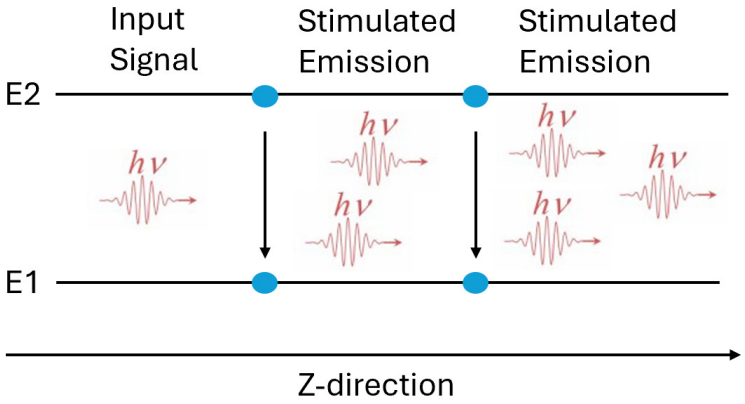


Figure 2.6: Optical signal amplification through stimulated emission, $h\nu$ represents an incoming/generated photon.

Even if we've obtained amplification we've also generated noise. This noise is called Amplified Spontaneous Emission (ASE). It is produced when carriers in an excited state (E_2) decay spontaneously to a lower energy level (E_1) releasing a photon. These spontaneously emitted photons are then amplified by the same gain medium used to boost the input signal as they travel through the amplifier. This phenomenon is considered noise because it is a random and incoherent process where the emitted photons have random phases, travel in various directions and are completely independent in respect with the input signal. When these noise photons reach a photodetector they mix with the signal to create intensity and phase fluctuations which limit the system's sensitivity and degrade the Optical Signal-to-Noise Ratio (OSNR). ASE can also represent a serious risk to the physical integrity of the amplifier itself in high-power regimes. In the absence of a sufficiently strong input signal, or when the amplifier operates in a saturated regime, ASE can build up significantly

along the fiber length and accumulate enough power to cause physical damage. This can manifest as fiber fuse, a phenomenon in which the intense optical power density locally heats the fiber core above the silica melting point, initiating a self-sustaining damage front that propagates back toward the pump source permanently destroying the fiber. For this reason high-power amplifier systems must be carefully designed to manage ASE typically through the use of optical isolators, filters or by ensuring that the amplifier always operates with an adequate input signal level.

Thulium-Doped Fiber Amplifiers operate on a three-level energy scheme: electrons are pumped from the ground state (E_1) to an upper excited band (E_3) undergo rapid non-radiative decay to a metastable intermediate level (E_2) and finally return to the ground state via stimulated emission (Fig. 2.7). Despite this physical three-level structure TDFAs are conventionally modeled as effective two-level systems. This simplification (Fig. 2.6) is justified by the fact that the non-radiative relaxation from the higher state to the metastable level is basically instantaneous compared to the comparatively long lifetime of the metastable state. As a result, the population of the upper pumping band remains negligible at all times, and the amplifier dynamics are entirely governed by the exchange between the metastable level and the ground state. The two-level approximation therefore introduces no meaningful loss of accuracy. The actual energy level structure of the Thulium ion is illustrated in Fig. 2.7.

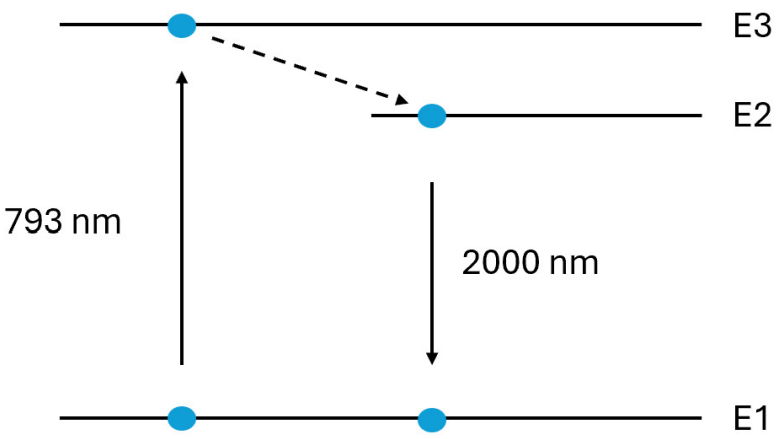


Figure 2.7: Diagram of Thulium energy levels, dashed line between E_3 and E_2 represents a non-radiative decay (heat).

After the explanation of the physical principle behind the light amplification it is important to explain through which components it is possible to achieve said amplification. It is already been mentioned that the amplification occurs inside a doped fiber but, as today, there are several different active fiber that we can choose. Before describing the possible geometries a brief explanation about why a double-cladding architecture are used is needed. In a standard single-mode fiber the pump light is coupled directly into the core along with the signal. This approach works well when using single-mode pump sources, such as laser diodes emitting in a single spatial mode, which can be efficiently coupled into the small core (typically 5 µm to 10 µm in diameter). However, high-power pump sources emit light from a much

larger aperture and cannot be efficiently coupled into such a small core. Double-cladding fibers solve this problem by introducing a second guiding region. The pump is coupled into the inner cladding, which has a much larger cross-sectional area and a higher numerical aperture, allowing efficient coupling of high-power pump sources. The pump then propagates through the inner cladding and is gradually absorbed by the doped core as it repeatedly crosses it while the signal remains guided exclusively in the core. This architecture, therefore, decouples the requirements on the pump and signal beams. The signal can still propagate in a single spatial mode within the core, preserving beam quality, while the pump can be a high-power source. The result is a configuration that simultaneously achieves high pump power and high output beam quality which is the key advantage of double-cladding fibers over single-cladding designs. Fig. 2.8 shows some of the possible fibers geometries that can be used to amplify light. It is easy to spot that the core, in almost all the cases, is placed right in the middle of the fiber while the inner claddings take quite exotic forms. The choice of inner cladding shape directly influences the pump absorption efficiency. Irregular geometries help break the rotational symmetry preventing the formation of helical modes that would otherwise propagate without ever intersecting the core thus reducing the effective pump-to-signal coupling.

For the work presented in this thesis the configuration (a) of what is reported in Fig. 2.8 was chosen. While this geometry is the simplest among those illustrated, it still allows us to obtain the required amplification.

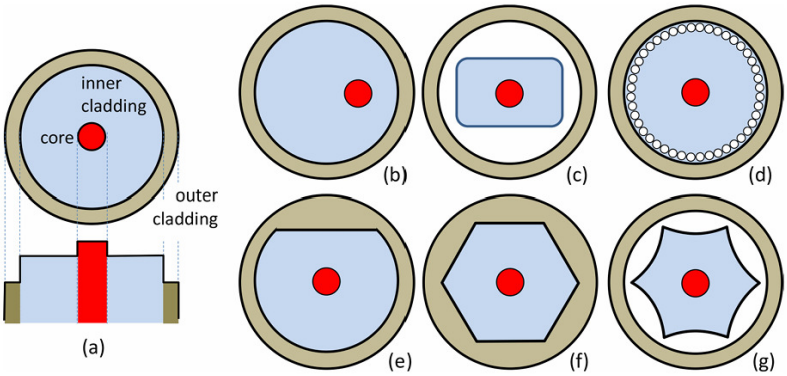


Figure 2.8: Different types of double cladding fiber, the different inner cladding shapes allow a different superposition of the pump modes on the core [4].

Lastly, the reader may ask why a TDFAs is used instead of collimating several different laser diodes. The problem is the beam quality. Beam quality describes the spatial properties of a laser beam and its ability to be focused and it is commonly quantified through the beam propagation factor M^2 which compares the divergence of a real beam to that of an ideal Gaussian beam. For an ideal Gaussian beam M^2 has a value of 1. Real beams always have $M^2 > 1$ meaning they diverge faster and are harder to focus than the ideal case. In high-power applications this means that the target receives a beam with lower power density and coupling efficiency into downstream optical components is reduced. A TDFA naturally provides excellent beam quality because the waveguide structure of the fiber constrains light propagation and, in single-mode or near single-mode operation, suppresses higher-order transverse modes resulting in output beams with M^2 values typically close to 1. A

system based on multiple collimated beams cannot easily achieve comparable performance. Incoherent beam combining increases total output power but degrades the spatial profile and focusability while coherent beam combining, although capable of preserving beam quality in principle, requires precise control of the relative phase, alignment and stability of each individual channel greatly increasing system complexity. For these reasons a TDFAs represents the most practical solution offering a favorable balance between output power, beam quality, compactness and system stability.

2.4 MOPA laser

A MOPA laser is a specific architecture designed to produce high-power coherent radiation by decoupling the initial laser signal generation from its amplification. This configuration consists of a master oscillator (seed), which generates a low-power highly coherent beam, and a power amplifier (often structured as a cascade of multiple stages) that boosts the signal's power while preserving its original characteristics. A primary advantage of the MOPA design is that it is far easier to control and tune the parameters of a low-power seed, for example by adjusting the driving current, and then amplify it than it is to generate a high-power beam and subsequently modify its properties. Many modern systems are implemented entirely with fiber technology providing a compact and robust design that resists external environmental factors and avoids the complexities of aligning bulk optics. In high-power fiber implementations the design must also mitigate nonlinear effects such as SBS and Stimulated Raman Scattering (SRS) which can limit the achievable output power [25]. Moreover, due to the high gain achievable by these amplifiers it is important to mitigate all the back reflections that may originate inside the system. This reflections (in particular back-reflections) can propagate back through the chain and destabilize or damage components. For this reason it is important to implement strategies like Faraday isolators (difficult in high power scenarios [26]) or optical isolators which are a better choice in those scenarios that require an high isolation ratio. Furthermore, to ensure high signal quality it's possible to incorporate optical band-pass filters between stages to suppress ASE which can, otherwise, limit the tuning range and power scaling of the system [27–29]. One problem of the MOPA design is that the amplifier acts as if it is an energy reservoir for the signal. This behavior lead to a condition called "gain saturation" whenever a pulse extracts a significant fraction of the stored energy. What happens is that the overall gain drops and the pulse gets distorted. To avoid or, in the worst case, limit this phenomenon the seed pulse shape can be pre-tailored in such a way to obtain the desired output profile after the amplification [30]. Thank to this architecture MOPA systems offer a good versatility. The seed can be independently optimized for peak emission, linewidth, pulse duration and repetition rate while the amplifier chain handles power scaling without compromising beam quality. For these reasons MOPA laser are used in several different applications such as Light Detection and Ranging (LIDAR)/remote sensing and medical imaging [31,32].

Fig. 2.9 shows the setup. The seed and the pump are located in the leftmost part of the figure, for both of them are reported underneath the symbol the typical wavelength emission. As said before isolators are needed to avoid back-reflections

and thus damage to the seed or pump diode. The passive optic fiber is represented as the orange line whereas the active fiber made of Thulium atoms (Tm^{3+}) is represented as a blue line. The active fiber is modelled as a loop because, in order to get a good amplification, few meter of it are required and, generally speaking, the fiber is set up in a coil to reduce its footprint and avoid damages. The coupler is mandatory in order to correctly couple the two signals inside the fiber, the seed signal must go inside the core where all the Thulium atoms are while the pump signal must be inserted in the first cladding of the fiber.

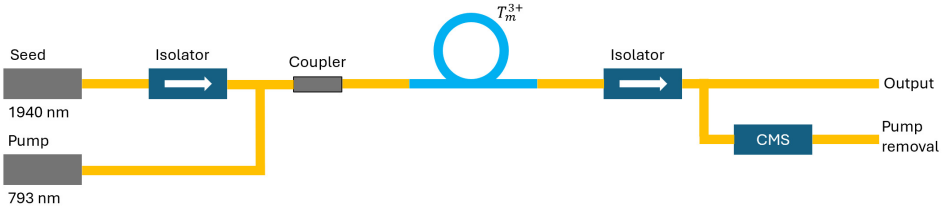


Figure 2.9: Setup for a single stage MOPA.

2.5 Applications of lasers

Since their invention, lasers have played an important role in scientific, industrial and medical applications. lasers can be found in several different fields:

- Industrial application such as cutting, drilling and welding. For the cutting and drilling lasers are used for their high repeatability and precision. For what concerns the welding part they're used for their ability to weld together identical or different metals which is quite hard to do with generic welding techniques
- laser's are used for material processing especially in 3D manufacturing and prototyping due to melting and sintering aspect of the technology. Another application can be found in micromachining thanks to the achievable micrometric/nanometric resolution.
- Medical applications such as surgery where lasers allow highly precise tissue cutting and cauterization and ophthalmology where they are routinely used for procedures such as retinal repair.
- Scientific applications including spectroscopy and metrology. In spectroscopy laser's light enables precise identification of atomic and molecular species whereas in metrology lasers are used in interferometric measurements.

Fig. 2.10 shows the various use cases for industrial lasers, which power is required and which laser technology is used to deliver that power.

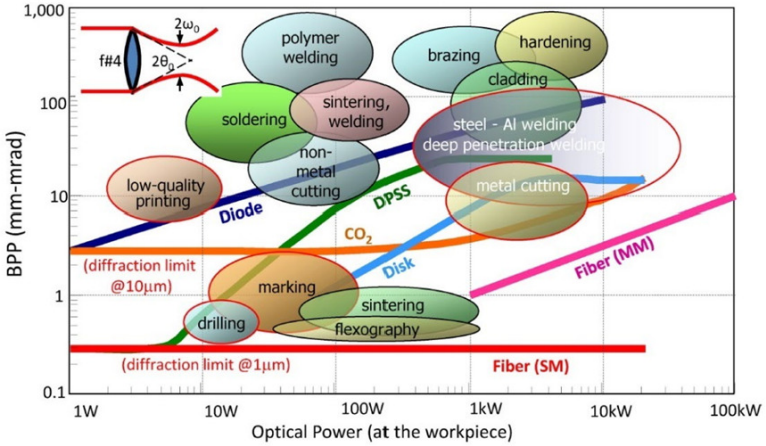


Figure 2.10: Power needed by different industrial application and which type of laser can be used to generate said power [5].

Another huge sector in which they're used is the medical/biomedical one. These lasers are increasingly being used in the biomedical field thanks to fact that the infrared light allow a good interaction with the organic matter. Among the currently available solutions the two most commonly used spectral regions are the one derived from the Ytterbium (1000 nm) and Thulium emission (2000 nm). Ytterbium lasers are characterized by a good beam quality and by the possibility to generate high power beams at the output. These laser generally emit in the spectral region between 1000 nm and 1100 nm, at these wavelengths there is a fair amount of penetration into organic matter. Ytterbium lasers are used in the biomedical field for imaging and diagnose in those cases where high accuracy and low thermal damages are needed. Thulium lasers on the other hand have an emission spectrum around 2 µm where a strong absorption peak of water molecules is located. This lead to a strong interaction with biological matter, a reduced penetration and a high accuracy during ablation. As a result, Thulium lasers can be used in surgery and in all those applications that require an high accuracy. Other fields in which Thulium lasers are used are: urology, dermatology, ophthalmology and dentistry for procedures such as tissue ablation, coagulation and phototherapy [33–39].

Fig. 2.11 shows the skin depth penetration of the two wavelengths described so far. Red arrows shows the penetration of 2000 nm Thulium emission [38] which is around 300 µm whereas the green arrows show the deeper penetration of 1000 nm Ytterbium emission [40] which goes up to 3.5 mm.

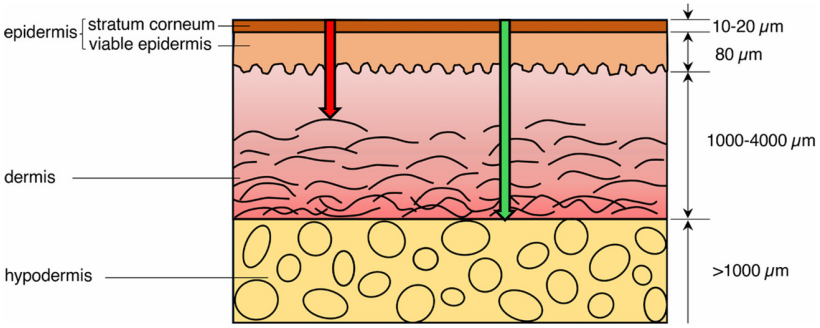


Figure 2.11: Skin depth penetration of 1000 nm (Ytterbium) and 2000 nm (Thulium) laser, image taken from [6].

Chapter 3

Thermal management

Thermal management play a key aspect during the design of any power device. If this heat is not properly dissipated the resulting temperature rise can lead to several undesirable effects including variations in refractive index, mechanical stress and degradation of optical components. In extreme cases excessive temperatures may damage the gain medium, coatings or fiber materials resulting in a degradation in device performance and reliability.

The only way possible to maintain the temperature within safe limits is to implement a cooling system. The choice os said system is limited to two different types: passive or active. Passive cooling solutions are the ones designed to work only by means of natural air convection. Generally, passive cooling is achieved by using metal plates or metal heatsinks, which radiates heat to the surrounding environment. On the other hand, active cooling relies on forcing a fluid, either air or a liquid, through the fins of a heatsink. Active cooling works better than passive cooling for different reasons. When air is used as a cooling fluid a channeled airflow provides a constant flow of cool air allowing the heat to be removed. A liquid instead has higher thermal conductivity and heat capacity than air allowing a better heat removal than the previous mentioned case.

For this thesis the goal is to implement a passive cooling solution rather than an active one. The reasons behind this choice are reported in the following list.

- Having an active power dissipation means that, at least, one fan is used to force air through the fins of the heatsink. The air flux created by the fan may be a source of different problem is those scenarios in which cleanliness plays a fundamental role such as operating rooms. For example, air moved by the fan can transport bacteria across the room, these bacteria may be the source of infections in the patient [41, 42].

- Compared with liquid cooling, passive cooling, offers greater long-term reliability, requires less maintenance and eliminates the need for pumps, fluid circuits and additional cooling fans. Its reduced number of components also enables a simpler, more compact and cost-effective design, while providing adequate thermal management for the intended application.

- A passive cooling system is considerably more cost-effective than an active one [43]. Moreover, the analysis of commercially available solutions revealed

several examples of passively cooled systems, supporting the investigation of this approach as an effective and cost-efficient solution for achieving the objectives of this work.

To perform the simulations the temperature of the air was set at 30 °C, the dissipated power was overestimated and not all the faces of the bodies involved in the simulation are assumed to be able to conduct heat. The adopted assumptions represent a worst-case condition compared with the expected operating scenario. Consequently, if the resulting temperature remains within the allowable range under these conditions, satisfactory thermal performances can reasonably be expected during laboratory testing. Furthermore, these assumptions simplify the implementation of the numerical model, improving computational stability and reducing simulation time without compromising the significance of the analysis. The result of these simulation will be discussed in the next paragraphs.
All the materials and their characteristics are reported in Tab. 3.1 whereas the power loads are reported in Tab. 3.2.

Table 3.1: Thermophysical properties of the materials used in the simulations

Material	**Thermal Conductivity** $\mathrm{W\,m^{-1}\,K^{-1}}$	**Specific Heat** $\mathrm{J\,kg^{-1}\,K^{-1}}$	**Mass Density** $\mathrm{kg\,m^{-3}}$	**Heat Capacity** $\mathrm{J\,m^{-3}\,K^{-1}}$
Copper	400	390	8960	3.49×10^6
Aluminum	238	900	2700	2.43×10^6
Thermal Paste	8.5	1000	2500	2.50×10^6
Glass	1	830	2500	2.08×10^6

Table 3.2: Volume, total power, and power density of the heat-generating components

Component	**Volume** $\mathrm{m^3}$	**Total Power** W	**Power Density** $\mathrm{W\,m^{-3}}$
laser package	1.03×10^{-4}	25	2.42×10^5
Fiber spool	1.61×10^{-6}	10	6.21×10^6

3.1 Simulation software and theoretical background

Thermal simulations can be performed by using different software but the working principle upon which all of them are built is the same. Among the most famous software present on the market today are COMSOL Multiphysics and Ansys. Both are well-established and validated tools for thermal FEM analysis but their usage is

subject to the purchase of a license. For this reason, while carrying out this work, a different approach has been chosen. The chosen software is SALOME MECA with the Code_Aster as a solver. SALOME MECA is the main Graphic User Interface (GUI) through which all the simulation details can be set whereas Code_Aster is the Finite Element Modelling (FEM) solver.

The FEM is a numerical technique used to obtain approximate solutions to boundary value problems governed by partial differential equations, such as the heat conduction equation. The body on which the simulation is to be performed, typically defined through a CAD model, is discretized into a finite number of smaller, simpler sub-domains called elements, connected at points known as nodes. This discretized representation is referred to as the mesh. Within each element, the unknown field (in this case the temperature) is approximated using interpolation functions defined over the nodal values. The governing differential equations are solved numerically, in this case by Code_Aster. In order to provide a solid starting point for the FEM software to start working on the problem a few steps must be followed:

- **Pre-processing** - The first data that must be provided to the solving software is the geometry of the bodies upon which the meshes have to be created. If the geometry is simple, it can be directly created inside the software but, generally speaking, other CAD tools, such as Fusion 360 or FreeCAD, are used to build a proper and accurate geometry of the body. After that, the geometry is imported in the main software that serves as a GUI and the mesh is created. Different meshes can be created, from simple triangles to polygon is important to choose the correct shape and size to avoid excessive solving time.

- **Physical problem definition** - The second step is to define all the materials, their physical characteristics and the loads applied to the bodies (Tab. 3.1 and Tab. 3.2 respectively show what has just been described). This step is crucial as the solver must know all the characteristics and all the power involved to correctly simulate the final temperature or the heat transient of the system.

- **Solving** - The solver creates the system of equations needed to solve the simulation. These equations vary from case to case due to their depending on whether the regime is steady-state or transient, on the boundary conditions, and on other factors.

- **Post-processing** - Once the simulation has finished the main software provides a section in which all results can be viewed, for example, as colored maps, graphs, or tables.

Having established the simulation workflow, the theoretical background underlying the heat transfer problem is presented in the following section. There are two equations used as building blocks. The first one, equation (3.1), is the Fourier's law which correlates the heat flux with the temperature gradient. Inside this equation the term q represents the heat flux whereas k is the thermal conductivity and T the temperature.

$$q = -k\nabla T \tag{3.1}$$

The second one, equation (3.2), describes the energy conservation inside an infinitesimal volume. ρ is the density, c_p the specific heat and $\dot{q}_{gen}$ is the volumetric source which represents the load previously described.

$$\rho c_p \frac{\partial T}{\partial t} = -\nabla \cdot q + \dot{q}_{gen} \tag{3.2}$$

When (3.1) and (3.2) are combined, while considering k as a constant, equation (3.3) is obtained.

$$\rho c_p \frac{\partial T}{\partial t} = k\nabla^2 T + \dot{q}_{gen} \tag{3.3}$$

This equation can be solved both in steady state and in transient regime. Considering the steady state case, represented by $\frac{\partial T}{\partial t} = 0$, the governing equation becomes the following.

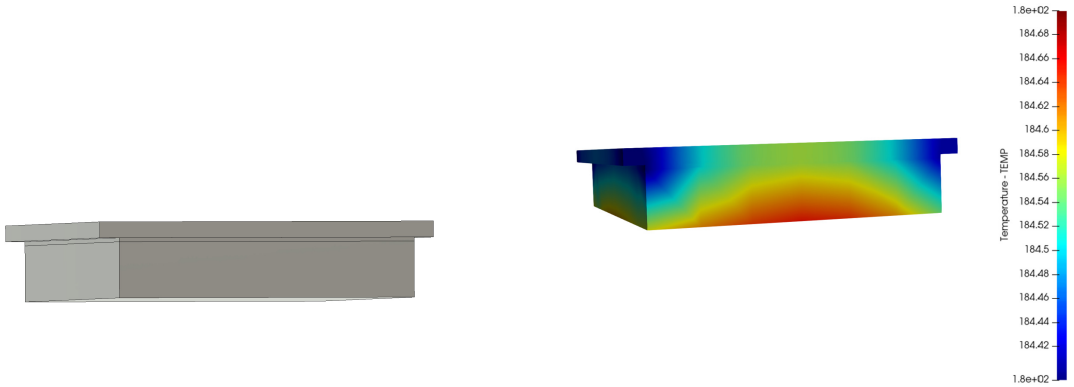
$$k\nabla^2 T + \dot{q}_{gen} = 0 \tag{3.4}$$

In the second case, the transient regime, the governing equation remains formally the same, as the time dependence is no longer zero. However, in the literature it is often found written in a different, equivalent form. What differs is the term $\alpha = k/(\rho c_p)$ which is called thermal diffusivity and represents the rate at which heat spreads throughout the material.

$$\frac{\partial T}{\partial t} = \alpha\nabla^2 T + \frac{\dot{q}_{gen}}{\rho c_p} \tag{3.5}$$

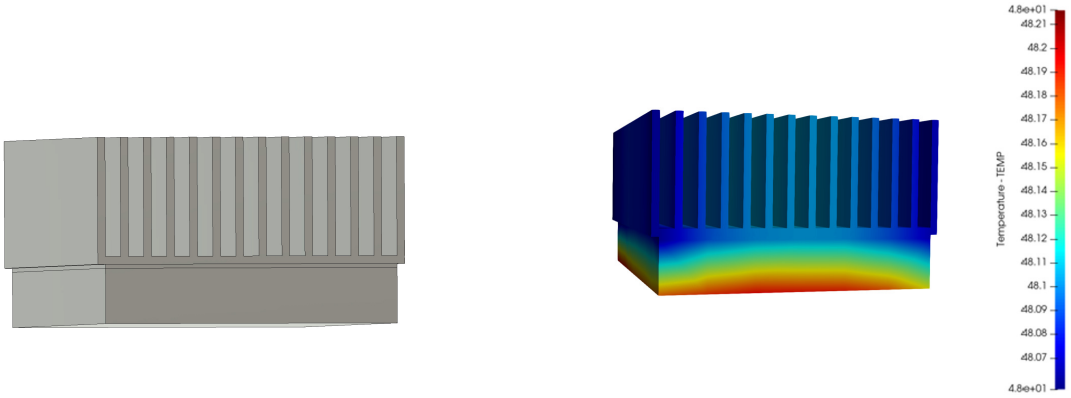
3.2 Heatsink vs generic plate

The first simulation aimed to determine whether, given the relatively low power involved, a dedicated heat sink was actually required or whether a simple copper plate would provide sufficient cooling. In order to simulate the system to different models were required. The first model, represented in Fig. 3.1a, shows the laser's package (bottom rectangle), the Thermal Interface Material (TIM) (middle layer) and the Copper plate (top rectangle). As displayed in Fig. 3.1b this solution is ineffective at effectively dissipate the heat, due to this reason the reached temperature was 180 °C. The second model, represented in Fig. 3.2a, uses a generic heatsink as a replacement to the Copper plate. The situation improved significantly as the temperature reached by the laser stayed below 50 °C which is a more reasonable working range. The result of the last simulation was used a starting point for the next simulations.



(a) (b)

Figure 3.1: 3D model (left) and Thermal simulation (right) of heat dissipation through Copper plate.



(a) (b)

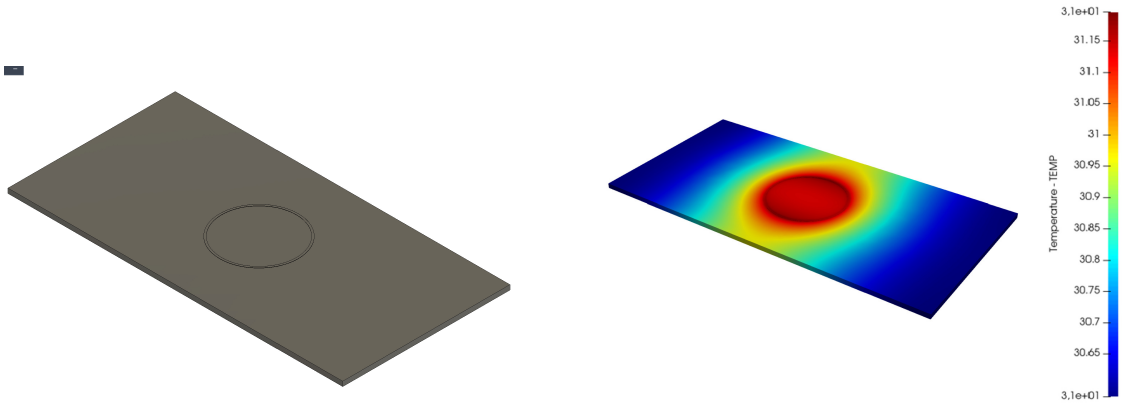
Figure 3.2: 3D model (left) and Thermal simulation (right) of heat dissipation through Copper Heatsink.

3.3 Fiber heat spreading

Generating 10 W of optical output requires roughly 20 W of input pump power, about 10 W are converted into heat and must be dissipated by the fiber. Since Thulium fibers are quite sensitive to temperature variations an additional thermal simulation was performed to evaluate the working temperature of the fiber. Fig. 3.3b shows that the fiber experiences only a very small temperature increment. As said before, the ambient air temperature in the simulation was set to 30 °C. Under a thermal load of 10 W the resulting temperature rise of the fiber is only about 1 °C showing that the chosen thermal management is more than sufficient.

The base serving as both the mechanical support and heat-dissipation medium for the fibre was based on a commercial Thorlabs component, whose specifications are reported in Tab. 3.3. The original model available on the manufacturer's website

includes numerous mounting holes. However, these geometrical features would have generated an excessively large number of mesh elements, significantly increasing the computational complexity of the simulation. The geometry was therefore simplified by modelling the base as a solid Aluminum component, while retaining the material properties and overall dimensions relevant to the thermal analysis. The fiber spool was modelled as a circular structure with a diameter of 20 cm and a thickness of 500 µm. This simplified geometry was designed to represent a coil comprising multiple turns of the TDFA fiber.



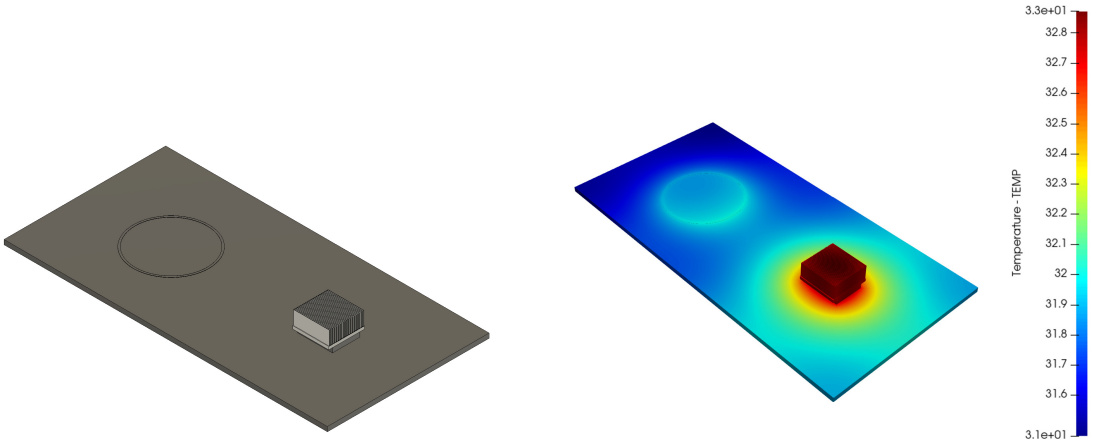
(a) (b)

Figure 3.3: 3D model (left) and Thermal simulation (right) of heat generated by the active fiber.

3.4 Fiber laser simulation

This simulation was performed to check two different things. First, we wanted to evaluate the thermal behavior of the system when both the laser and the optical fiber were mounted on the same Aluminum plate. And second, we wanted to check how the temperature of the laser would change when mounted onto the Aluminum plate. Due to good Aluminum thermal conductivity a decrement of the laser's temperature was expected. The results show that the temperature of the fiber remains essentially unchanged whereas the laser temperature decreases by approximately 15 °C. This can be explained by the fact that the Aluminum base acts as a sort of second heatsink allowing a better heat dissipation of the overall system. It should be noted that, although a TIM layer was inserted between the laser and the heatsink to improve thermal conductivity, the interface between the laser and the base involves no TIM layer. Comparing Fig. 3.2b and Fig. 3.4b can be appreciated the difference between how the laser's temperature decreased when the Aluminum base was added.

This simulation had another purpose which was to verify whether the proposed configuration could realistically be implemented in the laboratory or not. The results confirmed that the thermal conditions were acceptable, which allowed us to proceed with the purchase of the actual components.



(a) (b)

Figure 3.4: 3D model (left) and Thermal simulation (right) of the laser and active fiber positioned on top of an Aluminum plate.

3.5 Final simulation

A final simulation was carried out using the CAD models of the actual parts. The only component, in addition to the Aluminum base for reasons already described, modelled by hand was the laser due to the unavailability of its CAD file, the package dimensions were obtained from the datasheet. The material properties used in the simulation are reported in Tab. 3.1. The simulated components and their materials are the following:

Table 3.3: Components and materials of the simulated devices

Component	**Material**
Base plate	Aluminum
Fiber	Glass
TIM	Thermal Paste
laser	Aluminum
Heatsink	Aluminum

As said before, this simulation was performed to evaluate the thermal response of real components. The thermal load was evaluated again and updated with respect to the values reported in Tab. 3.2. The chosen laser has an Electrical-to-Optical Efficiency of 38%. The optical power needed at the output is still 10 W. Considering a fiber efficiency of 50% the laser must therefore emit 20 W of optical power. The problem is that, due to the low efficiency, in order to get 20 W at the output we need to inject an electrical power of $\frac{20\,\mathrm{W}}{0.38} \approx 53\,W$. Since the emitted power is 20 W the remaining power must be dissipated as heat by the package, the power emitted as heat amounts to $53\,\mathrm{W} - 20\,\mathrm{W} = 33\,\mathrm{W}$. The last difference with respect to the previous simulations concerns the volume of the laser package which has reduced. All these parameters are summarized in Tab. 3.4.

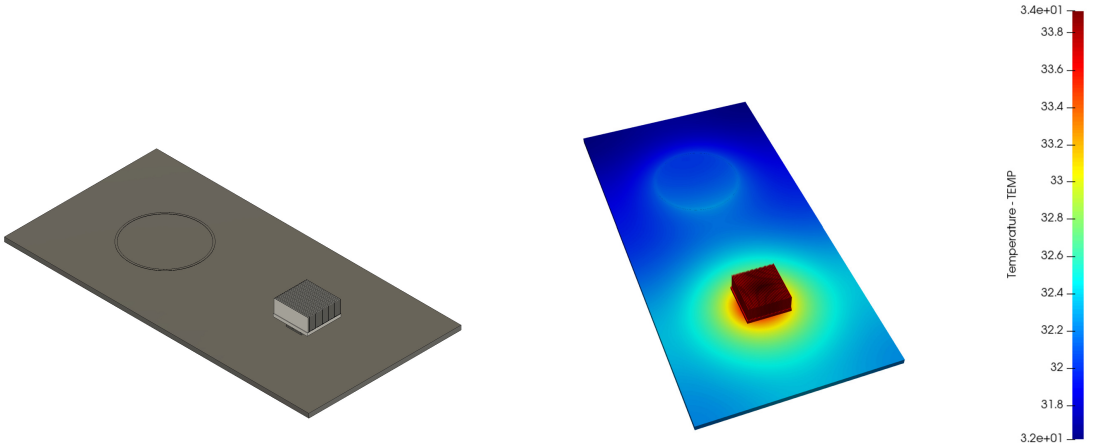
Table 3.4: Volume, total power, and power density of the heat-generating components

Component	**Volume**	**Total Power**	**Power Density**
	m^3	W	$W\,m^{-3}$
laser package	5.09×10^{-5}	33	6.49×10^5
Fiber spool	1.61×10^{-6}	10	6.21×10^6

Fig. 3.5a shows the final CAD models that was used in the simulation. The base plate, the fiber and the heatsink are the same with respect to the previous simulation (Fig. 3.4a). Only the laser and, consequently, the TIM layer was modified. As shown in Fig. 3.5a the laser is not visible as it is clamped between the base plate and the heatsink.

Fig. 3.5b shows the result of the simulation. What was obtained is similar to what is reported in Fig. 3.4b. Even if the thermal load was increased and the volume was decreased the system is able to effectively dissipate all the heat generated by the laser. The temperature has increased by only 1 °C. This is an acceptable increment as the operating temperature is only 4 °C above the air temperature. Working at this temperature won't damage in any way the laser or the components putted inside the package such as the optical elements.

Lastly, an active cooling system was simulated in order to provide a reference point against which the results obtained from passive cooling could be compared. This is important because laser diodes must remain below a given temperature to avoid damage to the internal optical components and, more specifically, to the adhesives holding the assembly together. Another aspect monitored during the laboratory data collection was the heating/cooling transient and how the cooling system affected it. Comparing Fig. 3.5b with Fig. 3.6 the temperature reached by the laser/heat sink system is lower than that reached with passive cooling alone. Another difference lies in the fact that, with active cooling, the entire plate reaches the same temperature. This is because water conducts heat better than air and is therefore able to remove heat more effectively. The fiber also reaches a lower temperature when active cooling is used. Fig. 3.6 shows only the simulation and not the CAD model as it was used exactly the same model reported in Fig. 3.5.



(a) (b)

Figure 3.5: 3D model (left) and Thermal simulation (right) of the complete system with the proper CAD models and materials.

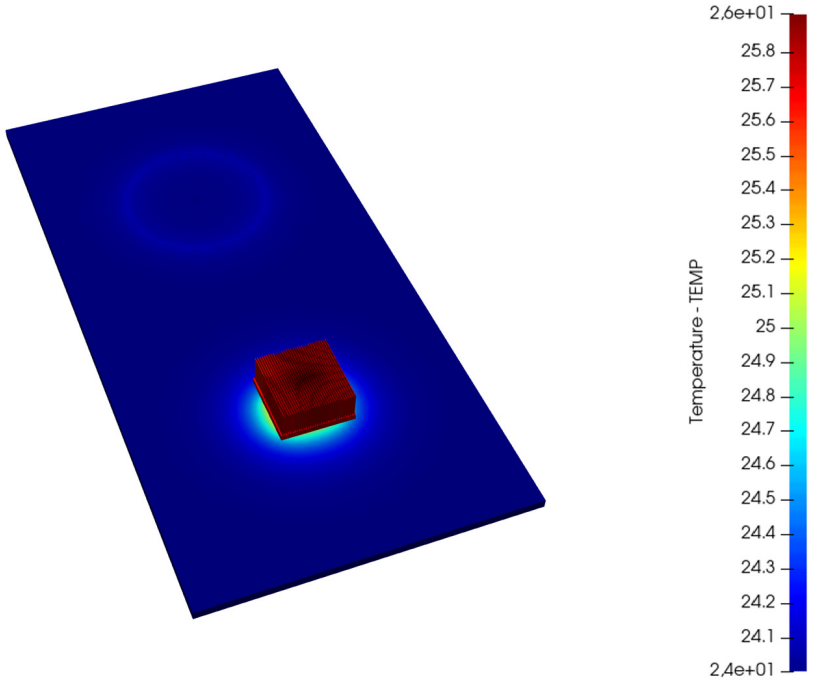


Figure 3.6: Thermal simulation of the complete system with the proper CAD models and materials dissipated by an active cooling device.

3.6 Experimental results

3.6.1 Thermal response under active and passive cooling

To verify that the results obtained in the thermal simulations were consistent with reality a FLIR thermal camera was used during the tests to monitor thermal behavior and capture images of the system. The system's temperature was monitored

under two cooling conditions: a passive air-cooling solution and an active water-cooling setup, the latter providing a reference case for comparison. Both tests were divided into three phases: in the first phase the laser was driven at 0.8 A, in the second phase the driving current was raised to 2.8 A and in the third phase the laser was switched off and the cooldown behavior of the system was observed. Each phase lasted 10 min.

The results of the first test are reported in Fig. 3.9a, with a corresponding thermal image of the setup shown in Fig. 3.7. Fig. 3.9a shows the passive-cooling thermal behavior of the laser diode and its driver, plotted as temperature versus time. As soon as the laser was driven the temperature began to rise reaching a value of approximately 30 °C for both components. By the end of the second phase the temperature had reached approximately 36 °C which is 2 °C higher than the value predicted by the simulation reported in Fig. 3.5b. This discrepancy is due to the fact that the simulation assumed an ambient temperature of 30 °C whereas the actual ambient temperature during the experiment was 33.5 °C. Taking into account the ambient temperature of the room in which the experiment was performed, as well as the observed system behavior, it can be concluded that the simulated behavior is correct and closely resembles the real behavior of the system. Lastly, the measured peak temperature of 36 °C remains within the 40 °C maximum allowable operating temperature for the laser diode and driver confirming that passive cooling alone is sufficient to keep the system within safe operating limits even at the highest tested drive current.

The second test was intended to validate the simulation and to characterize how the system would behave under active cooling. As shown in Fig. 3.9b the maximum temperature reached is roughly 8 °C lower than in the passive-cooling case. Moreover, a comparison between Fig. 3.6 and Fig. 3.8 shows a good agreement between the simulated and the measured data. The temperature reached by the plate during the laboratory test is essentially the same as the one obtained in the simulation while the laser reached a temperature about 2 °C higher than predicted. This small discrepancy can be attributed to the ambient temperature during the test, which was higher than the one assumed in the simulation. The initial rise followed by a drop in temperature, visible at the beginning of the plot, is due to the activation of the chiller. Furthermore, Fig. 3.8 confirms that the overall temperature under active cooling is lower than that observed in Fig. 3.7.

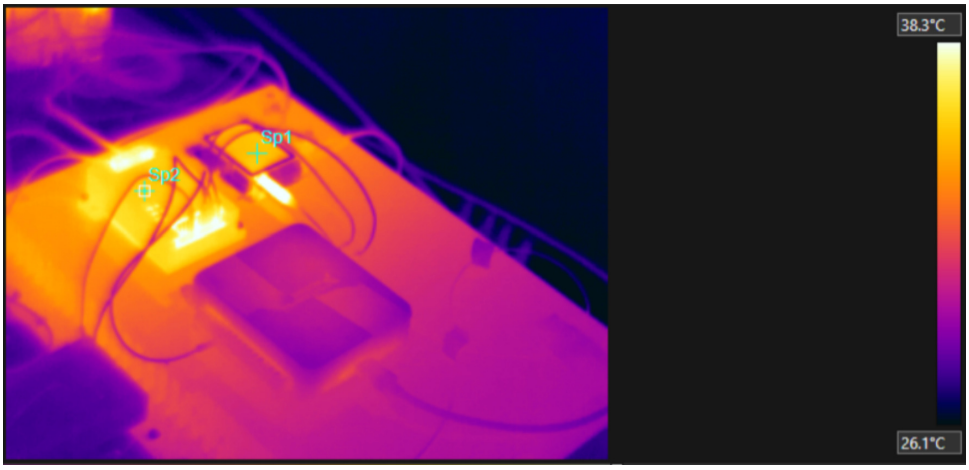


Figure 3.7: Temperature reached by the laser diode and the driver module with a passive cooling system capture with a thermal camera, Sp1 corresponds to the laser diode and spot Sp2 corresponds to the driver.

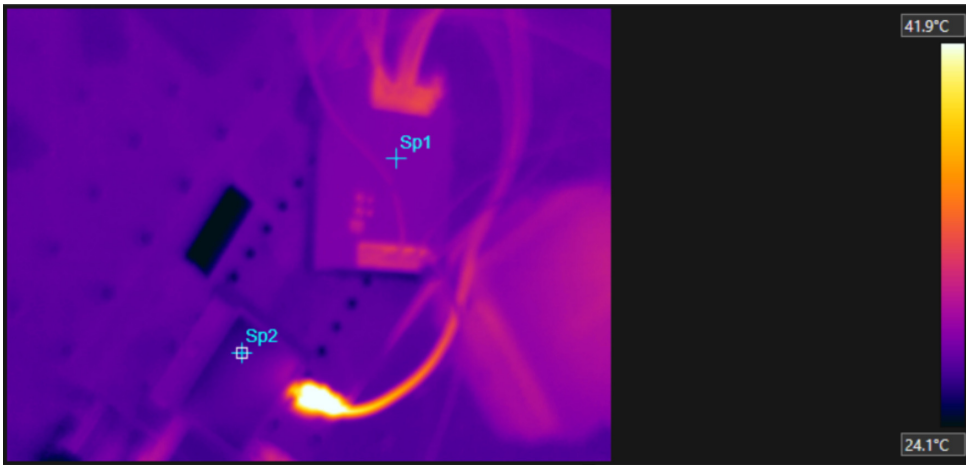


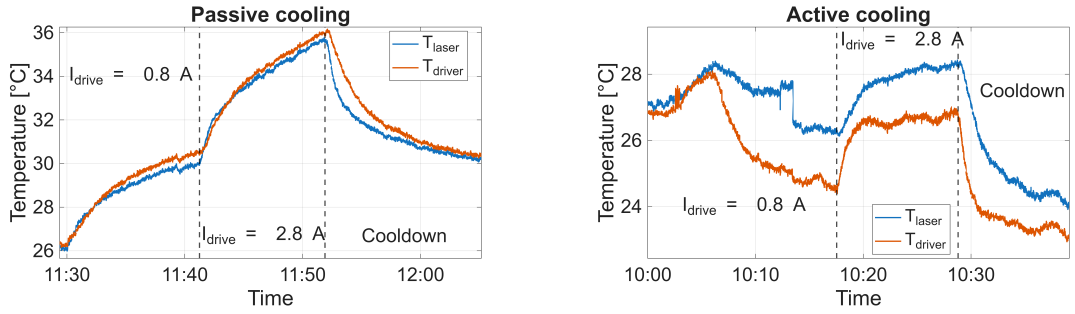
Figure 3.8: Temperature reached by the laser diode and the driver module with an active cooling system capture with a thermal camera, Sp1 corresponds to the driver and spot Sp2 corresponds to the laser diode.

3.6.2 Dynamic thermal behavior

To conclude the chapter on thermal simulations, a comparison is made between the transients obtained experimentally using passive and active heat dissipation systems and those obtained through simulation. The temperature transients experimentally measured during the laboratory test session are reported in Fig. 3.9. As already explained, the passive cooling solution is the one of actual interest, whereas the active cooling system is used only for comparison. Looking at Fig. 3.9a, it is noticeable that the laser and driver curves closely match each other. On the other hand, Fig. 3.9b shows the temperature transients obtained with an active cooling solution. In this case the two curves are separated by an offset of approximately 1 °C to 2 °C, depending on the drive current. The thermal behavior of the laser and

driver is similar, exhibiting a comparable steepness and plateau-like characteristic. The main difference between Fig. 3.9a and Fig. 3.9b is the maximum reached temperature, as was explained before, but, most importantly, the fact that the active cooling solution shows a plateau, which is not present in the passively dissipated system. This behavior can be explained by the fact that water is a better heat conductor, so the system reaches thermal equilibrium faster.

Thanks to the collected data, a comparison between the simulated temperature transient behavior and the real one can be performed. This comparison is shown in Fig. 3.10, the graph shows a good match between the simulated transient and the real one. There are some discrepancies, such as the maximum reached temperature and the shape of the curve. These differences can be attributed to the simulated system being similar, but not identical, to the real one, and to the ambient conditions in which the experimental evaluation took place, which also play a fundamental role. The strength of this simulation lies in the current-based behavior of the system: the temperature correctly increases as the laser's input power increases, and then, when the power is removed, the temperature starts to decrease. Despite the presence of the mentioned differences, the overall simulated behavior is correct, as the curve matches the trend of the experimental one. For this reason, the simulation can be considered valid.



(a) (b)

Figure 3.9: Thermal behavior of the pump laser diode and driver electronics under active (a) and passive (b) cooling.

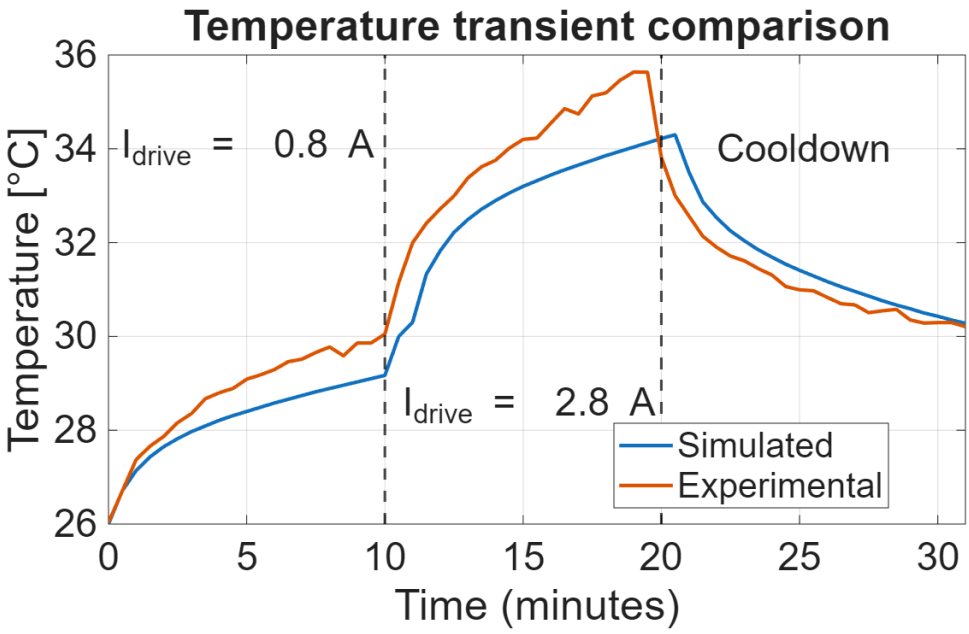


Figure 3.10: Comparison between the simulated and experimental heating and cooling temperature transient for the passive cooling system.

Chapter 4

TDFA simulations

As stated before this thesis aims to design, simulate and characterize a fiber laser capable of delivering a nominal power of 10 W at 1940 nm. Starting from a seed optical power of 10 mW, the system must provide a gain of 30 dB to achieve the desired output power. As discussed in Chapter 2, the amplification stage is implemented using a TDFA. This gain places the system firmly within the high-power amplification regime, where nonlinear and thermal effects must be carefully considered. Moreover, the complex spectroscopic and dynamical properties of Thulium ions introduce several design challenges. Therefore, numerical simulations are required to identify potential issues and optimize the system parameters before the experimental setup is constructed. This optimization process centers on three key design parameters, discussed in detail below.

- **Active fiber length** - An active fiber that is too short will result in insufficient pump absorption and consequently inadequate gain whereas an excessively long fiber can lead to re-absorption of the amplified signal. The simulations aim to identify the fiber length that maximizes the output power while maintaining a stable and efficient operating regime.
- **Number of amplification stages** - Depending on the gain saturation behavior of the active fiber and the constraints imposed by nonlinear phenomena, a single-stage amplifier architecture may not be sufficient to reach the target output power. The simulations were therefore used to determine whether or not a single stage is enough.
- **Nonlinear effects thresholds** - Unlike the previous two, this is not an independent design parameter but a constraint that emerges from them: both the active fiber length and the number of amplification stages directly affect the onset of nonlinear phenomena, which in high-power fiber systems can impose severe limitations on the achievable output power. Among these, SBS is a primary concern, as it can cause significant backscattering of the signal, leading to power clamping or, in the worst case, damage to the fiber. The simulations allow us to estimate the SBS threshold, guiding the choice of the previous two parameters so that the amplifier operates within safe operational boundaries.

Biomedical applications of Thulium-doped systems often require operation in pulsed regime rather than continuous wave. For this reason, once the system has been

optimized in CW operation, the analysis is extended to the pulsed regime in order to verify that the system performs correctly under these operating conditions as well. Different surgical techniques require different pulse trains which differ in pulse length and repetition rate. By tuning these parameters, the same setup can be used to perform different surgical operations. To achieve optimal results, the system must be able to generate all of these pulse trains. The characteristics of these pulses are reported in Tab. 4.1.

When soft tissue ablation, or hemostasis, has to be performed the pulse duration plays a critical role. Pulse duration determines how far with respect to the probe insertion point the coagulation will extend and, furthermore, determines the area inside which the tissue will be damaged. Shorter pulses tend to confine the thermal effect more precisely to the target point whereas longer pulses allow a wider coagulation zone that can be exploited for hemostatic purposes. Regarding lithotripsy application (kidney stone ablation) Thulium laser has demonstrated excellent performances thanks to its higher absorption coefficient in water at 1940 nm and its capability to operate at pulse repetition rates up to 2000 Hz. These characteristics allow the generation of very fine stone dust that can be expelled by the body without the need for fragment retrieval surgery. In this working regime low pulse energies are combined with high repetition rates so that the average power delivered to the stone remains sufficient for efficient ablation while minimizing retropulsion (the migration of stone fragments upward into the kidney during lithotripsy). Lastly, in the context of neurosurgical hemostasis, pulse duration in the range of 10 ms to 500 ms at a repetition rate of 1 Hz is effective for non-contact blood vessel occlusion on porcine brain tissue achieving a coagulation efficiency of up to 100%. In this study the laser's emitted power was approximately 15 W, assuming that coagulation efficacy depends primarily on the thermal energy delivered rather than on instantaneous power, a laser power of 10 W would be expected to achieve comparable results at a proportionally longer exposure time. The non-contact modality is particularly advantageous in neurosurgery as it avoids the mechanical trauma associated with the use of bipolar forceps which can produce tissue sticking and carbonization. All the data written in this paragraph and in Tab. 4.1 were retrieved from [10–13].

Table 4.1: laser's parameters for Ablation and Hemostasis

Technique	**Pulse duration**	**Repetition rate**
Ablation (soft tissues)	10 ms	20 Hz to 50 Hz
Ablation (kidney stone)	0.05 ms to 10 ms	10 Hz to 500 Hz
Hemostasis	100 ms to 500 ms	1 Hz

4.1 Physical quantities relevant to laser-tissue interaction

While pulse duration and repetition rate determine the temporal delivery pattern of the laser energy, a complete characterization of the light-tissue interaction requires

distinguishing between several related but physically distinct quantities: pulse energy, peak power and average power. Although these parameters are often interchanged in the clinical literature each of them plays a different role in the ablation or coagulation process. All the data written in this paragraph were retrieved from [10–13].

Pulse energy is the energy delivered by a single pulse. This parameter, together with the illuminated area, determines whether or not the ablation threshold is exceeded. Each technique requires a different amount of energy to be delivered, Tab. 4.2 lists the various energy ranges needed. The listed energy values were retrieved from empirical studies and not from theory. For example, for hemostasis, high-energy long-duration pulses were chosen to mitigate heat damage to the surrounding tissue, while low-to-high-energy high-repetition-rate pulses are useful to break kidney stones into a very fine dust which is faster and easier to expel. The illuminated area also plays an important role during surgery as the same amount of energy delivered over a smaller or larger area produces considerably different effects. The energy density actually delivered to the tissue surface is called "fluence". For a given amount of energy as the illuminated area gets smaller the energy density increases ensuring greater effectiveness in ablative procedures which requires high energy density. For example, incision of the ureter and bladder neck is performed with fluences in the range of $35\,\mathrm{J\,cm^{-2}}$ to $88\,\mathrm{J\,cm^{-2}}$ and $53\,\mathrm{J\,cm^{-2}}$ to $71\,\mathrm{J\,cm^{-2}}$ even if the corresponding pulse energies was only in the range 100 mJ to 250 mJ. The high energy density can become a problem when small-core fibers are employed, for example for flexible ureteroscopy, as the same pulse energy gets concentrated in a smaller area increasing therefore the risk of exceeding the fiber tip damage threshold. For this reason it is important to consider the fluence during the design fase in order to avoid damages during the actual surgery.

Table 4.2: Pulse's energy for Ablation and Hemostasis, [10–13]

Technique	**Pulse energy**
Ablation (soft tissues)	100 mJ to 250 mJ
Ablation (kidney stone)	25 mJ to 6 J
Hemostasis	1.5 J to 7.5 J

For what concerns the pulse's power two different quantities have to be considered: peak power and average power. Peak power is defined as $P_{peak} = E/\Delta t$ where E is the pulse's energy and Δt is the pulse length which means that for a fixed amount of delivered energy, shortening the pulse duration increases the peak power delivered to the tissue, even though the total energy deposited remains unchanged. For a MOPA system the peak power usually corresponds to the power rating of the seed laser whereas in a Q-switch configuration can reach the magnitude of several kW. When the pulse duration is shorter than the characteristic thermal diffusion time of the heated volume, the interaction is said to occur under thermal confinement, and the resulting temperature rise remains localized to the region where the light was absorbed. An analogous condition, stress confinement, is reached when the pulse duration is shorter than the time required for a thermoelastic stress wave to propagate across the heated volume; under this condition, the internal stresses generated cannot relax during the pulse itself, favoring mechanical fracture of the

target over gradual thermal damage. Consequently, two pulses carrying the same energy but different durations can produce markedly different outcomes: a long, low-peak-power pulse tends to favor a gradual, photothermal interaction, whereas a short, high-peak-power pulse of equal energy can push the interaction into a photomechanical or explosive regime, with sharper spatial confinement of the effect and reduced residual thermal damage in the surrounding tissue. This is precisely the trade-off exploited across the different pulse trains reported in Tab. 4.1: hemostasis relies on long pulses of moderate peak power to promote a controlled, diffusion-limited coagulation zone, whereas lithotripsy relies on short, low-energy pulses delivered at high repetition rates, which combine confinement-favoring peak powers with a sufficient average power for efficient stone fragmentation. While peak power describes the instantaneous power delivered during a single pulse, it does not capture how frequently that pulse is repeated over time. This is quantified by the average power, defined as $P_{avg} = E \cdot f_{rep}$, where f_{rep} is the pulse repetition rate. Unlike peak power, which governs the physical regime of the light-tissue interaction, average power determines the overall throughput of the procedure namely the rate at which tissue can be removed or coagulated.

4.2 Theoretical principles and equations behind the simulation

The following section presents the equations required to perform the optical simulations. Although the energy-level diagram of the thulium ion was introduced previously, it is reported again here for ease of reference and modified to match the equation notation. The reported diagram shows the simplified Thulium energy levels for the same reasons explained in 2.3.

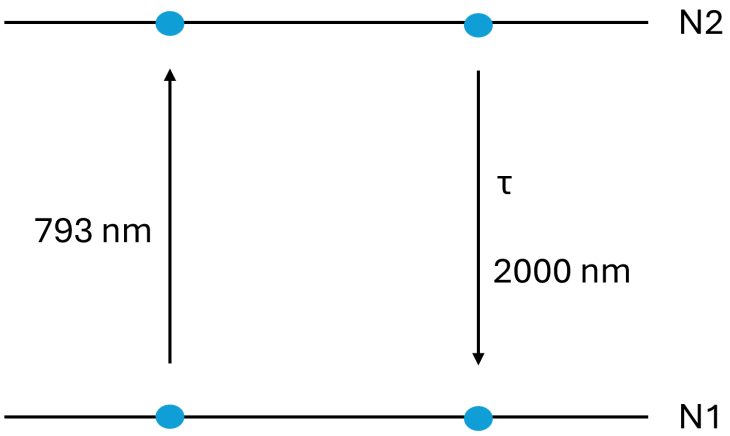


Figure 4.1: Diagram of the simplified Thulium energy levels, τ is the average lifetime of the electrons laying in the excited state.

In order to correctly simulate the fiber behavior and how the pulse propagates inside it we need two sets of different equations. The first one is the rate equation (4.1). This equation describes the electron population at a certain point inside the fiber

at a certain time instant. The leftmost term describes the temporal evolution of population of the excited state N_2 and the spontaneous decay of electrons returning to the ground state N_1 with an average lifetime of τ. This term is characterized by a partial derivative as the population in the excited state depends both on position along the fiber and on time. Under steady-state conditions (when the laser has been on for a while and nothing changes) this term is set equal to zero. P_p is the term that describes the pump signal, the notation $P_p^+(z,t) + P_p^-(z,t)$ accounts for both co-propagating and counter-propagating pump waves both contributing to the population inversion. The last term, the one described by the sum, is inserted to take into account the fact that the signal can excite more than one mode.

$$\begin{aligned}\frac{\partial N_2(z,t)}{\partial t} + \frac{N_2(z,t)}{\tau} = &\frac{\Gamma_p \lambda_p}{hcA_c}\left[\sigma_{ap}N_1(z,t) - \sigma_{ep}N_2(z,t)\right]P_p^-(z,t) \\ &+ \sum_k \frac{\Gamma_k \lambda_k}{hcA_c}\left[\sigma_{ak}N_1(z,t) - \sigma_{ek}N_2(z,t)\right]\left(P_k^+(z,t) + P_k^-(z,t)\right)\end{aligned} \tag{4.1}$$

The second set is composed by (4.2) and (4.3), while the previous rate equation describes what happens to the atoms in the medium these equations describe what happens to the photons as they travel along the fiber. Starting from (4.2) we can see that there is the term $\pm\frac{\partial P_p^{\pm}(z,t)}{\partial z}$ which describes how the power varies along the propagation direction, the sign $\pm$ is placed there to take into account both the co-propagating and the back-propagating waves. The second term $\frac{\partial P_p^{\pm}(z,t)}{\partial t}$ describes how the power varies over time. Looking at the right-hand side of the equation there is $\Gamma_p\left[\sigma_{ep}N_2(z,t) - \sigma_{ap}N_1(z,t)\right]$ which describes the exchange of energy with the atoms. Since, for the pump, absorption ($\sigma_{ap}N_1$) typically dominates over emission this term is almost always negative which means that the pump transfers energy to excite the electrons. The last term $\alpha_p P_p$ represents the intrinsic losses of the fiber.

$$\begin{aligned}\pm\frac{\partial P_p^{\pm}(z,t)}{\partial z} + \frac{1}{v_p}\frac{\partial P_p^{\pm}(z,t)}{\partial t} = &\Gamma_p\left[\sigma_{ep}N_2(z,t) - \sigma_{ap}N_1(z,t)\right]P_p^{\pm}(z,t) \\ &- \alpha_p\, P_p^{\pm}(z,t)\end{aligned} \tag{4.2}$$

The second equation (4.3) represents what was just described but for the signal, the only thing that differs from the previous equation is the term $2\sigma_{ek}\frac{hc^2}{\lambda_k^3}\Delta\lambda_k N_2$ used to describe ASE.

$$\begin{aligned}\pm\frac{\partial P_k^{\pm}(z,t)}{\partial z} + \frac{1}{v_k}\frac{\partial P_k^{\pm}(z,t)}{\partial t} = &\Gamma_k\left[\sigma_{ek}N_2(z,t) - \sigma_{ak}N_1(z,t)\right]P_k^{\pm}(z,t) \\ &- \alpha_k\, P_k^{\pm}(z,t) \\ &+ 2\sigma_{ek}\frac{hc^2}{\lambda_k^3}\Delta\lambda_k\, N_2(z,t)\end{aligned} \tag{4.3}$$

Lastly, equation (4.4) expresses the conservation of the total ion population. Since only a two-level system is considered, at any given time instant the sum of the

population in the ground state N_1 and in the excited state N_2 must equal the total ion population N_{TOT}.

$$N_{TOT} = N_1(t) + N_2(t) \tag{4.4}$$

4.3 RP simulations

RP Fiber Power is a powerful tool that can be used to design and simulate optical devices such as fiber amplifiers, lasers and other passive optical devices. Its functionality is well established in the optical world and it is very often considered the state-of-the-art software to use. The main problem with the RP Fiber Power ecosystem is its closed-source nature and the difficulty of using it in conjunction with external tools. For example, it is not possible to use the software inside an optimization routine written in an external language or with a different tool, forcing the optimization to be performed entirely inside the software, at the cost of several lengthy, separate simulations. Another problem is that the software does not allow other meaningful simulations to be performed, such as thermal ones. This is a significant limiting factor as, when working with high-power optical devices, good thermal management is required.

4.3.1 Optical simulations

The simulation was set up in order to simulate a single stage amplification with the characteristics reported in Tab. 4.3. The signal wavelength is λ_s and the pump wavelength is λ_p. The cross-sections describe the probability of photon-ion interaction, σ_{ap} and σ_{ep} are respectively the absorption and emission cross-sections at the pump wavelength while σ_{as} and σ_{es} are the same quantities but for the signal wavelength. The lifetimes τ_{21} and τ_{31} represent the spontaneous decay times respectively from the excited level to the ground one and from the metastable level to the excited one. Lastly, k_{1310} and k_{3101} are cross-relaxation coefficients.
The first aspect that has been checked was the optimal fiber length required to achieve the desired output power level. As shown in Fig. 4.2 several key observations can be made. Firstly, the amplifier works in such a way that, given the input power, the fiber is able to amplify through stimulated emission rather than spontaneous emission. It is possible to infer this from the fact that the output power increases. Secondly, amplifier saturation is visible at approximately 3 m. While the target output power is reached before saturation a secondary effect becomes evident. Once the fiber length exceeds the saturation point the signal begins to be re-absorbed by the active medium causing a reduction in the overall output power. Therefore, the optimal fiber length is defined as the one that maximizes the output signal power while simultaneously minimizing the residual pump power at the fiber end.

Table 4.3: Parameters of the simulation

Parameters	**Value**
λ_s	1940 nm
λ_p	793 nm
Signal power	15 mW
Pump power	28 W
σ_{ap}	$8.3410 \times 10^{-25}\,\mathrm{m}^2$
σ_{ep}	$3.3807 \times 10^{-25}\,\mathrm{m}^2$
σ_{as}	$0.1686 \times 10^{-25}\,\mathrm{m}^2$
σ_{es}	$4.1745 \times 10^{-25}\,\mathrm{m}^2$
τ_{21}	$540 \times 10^{-6}\,\mathrm{s}$
τ_{31}	$50 \times 10^{-6}\,\mathrm{s}$
k_{1310}	$3 \times 10^{-23}\,\mathrm{m}^3\,\mathrm{s}^{-1}$
k_{3101}	$0.084 \cdot 3 \times 10^{-23}\,\mathrm{m}^3\,\mathrm{s}^{-1}$

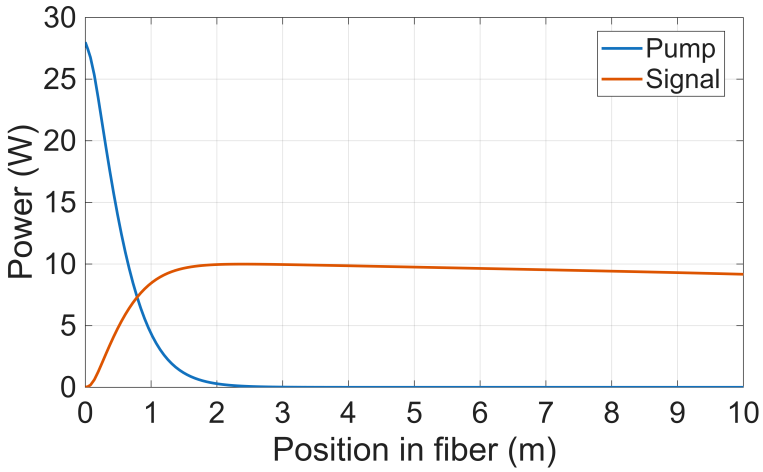


Figure 4.2: Evolution of the signal amplification and pump absorption as a function of the fiber length.

The second graph, reported in Fig. 4.3, shows the correlation between the input pump power and the output signal power. It is evident that for input pump power values below few Watts no amplification occurs. This threshold represents the minimum pump power required to achieve population inversion in the active medium. Above this value the output signal power increases approximately linearly with the pump power suggesting that the gain medium is not yet saturated over the range of pump powers considered. At 28 W of pump power the output signal reaches 10 W which is consistent with the results obtained in the fiber length optimization discussed previously.

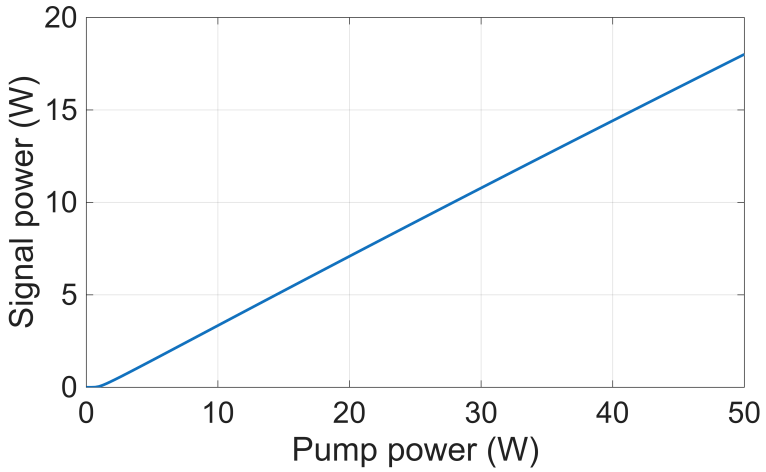


Figure 4.3: Correlation between input pump power and output signal power.

As discussed before, another problem that may emerge is the ASE. ASE varies in respect with the wavelength at which it is measured therefore a simulation aimed to check this behavior was performed. The results are reported in Fig. 4.4, two peaks can be observed but the one of our interest is the one centered around 1900 nm. Even if the some ASE is present in the system it doesn't represents a problem as it has a overall power that is several orders of magnitude smaller than the amplified signal, the signal's output power is 40 dBm while the ASE peak reaches at most −5 dBm.

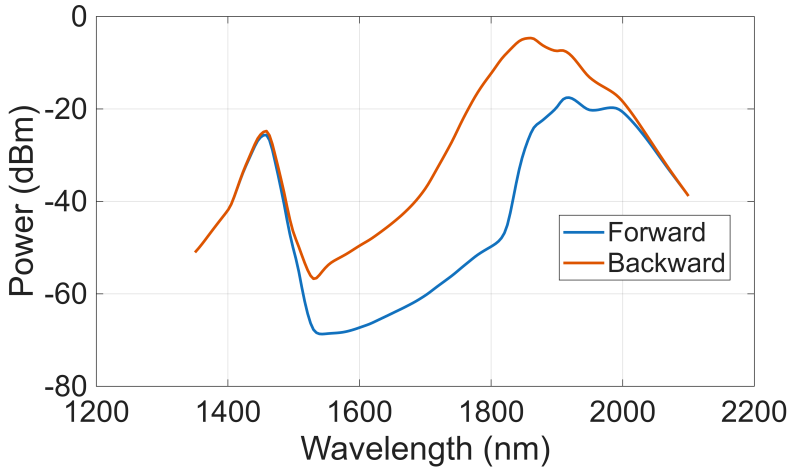
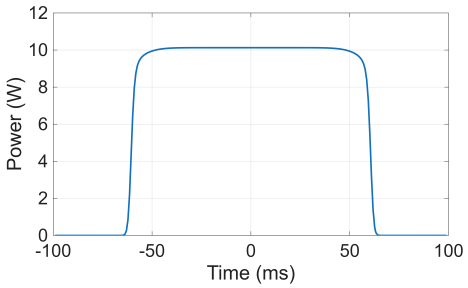


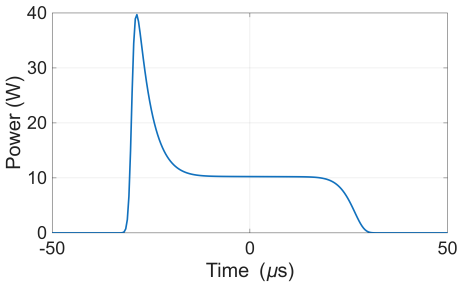
Figure 4.4: ASE spectrum between 1350 nm and 2100 nm [7].

After verifying the correct output power level and the ASE spectrum a dynamic simulation was performed. Several pulse configurations were simulated varying both the pulse duration and the repetition rate. A subset of the simulated pulses is displayed in Fig. 4.5. Specifically, Fig. 4.5a shows a 100 ms pulse with a repetition rate of 1 Hz, Fig. 4.5b shows a 0.05 ms pulse at a repetition rate of 500 Hz and Fig. 4.5c shows a 0.2 ms pulse at a repetition rate of 500 Hz. The values for pulse duration and repetition rate were taken from Tab. 4.1. These simulations were performed to verify two aspects: the shape of the amplified pulse and whether

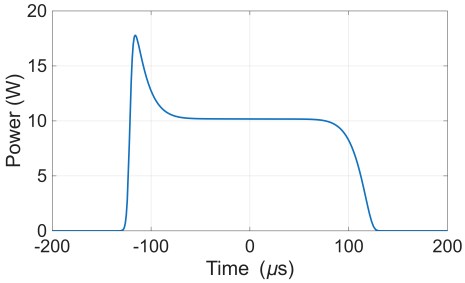
or not SBS would take place. Regarding the pulse shape the output waveform is correct. The overshoot visible at the leading edge in Fig. 4.5b and Fig. 4.5c is not a numerical artifact but rather a phenomena that occurs when all the energy stored inside the cavity is released all at once. On the other hand, regarding SBS, in some cases the computed values exceed the acceptable threshold of 90 dB. What was found is that for pulses between 0.05 ms than 0.2 ms the SBS reaches values up to 190 dB which is way bigger than imposed limit but all the other pulses stay below the limit. This amplifier configuration reached approximately 55 dB in the case of Fig. 4.5a, 188 dB in the case of Fig. 4.5b and 85 dB for Fig. 4.5c. These results shows that with this setup the shortest pulse length that can be achieved is 0.2 ms as shorter pulses will trigger SBS. A more detailed explanation on what is SBS and its origins will be reported in the next chapter 4.3.2.



(a) Single pulse with pulse duration of 100 ms and repetition rate = 1 Hz



(b) Single pulse with pulse duration of 0.05 ms and repetition rate = 500 Hz

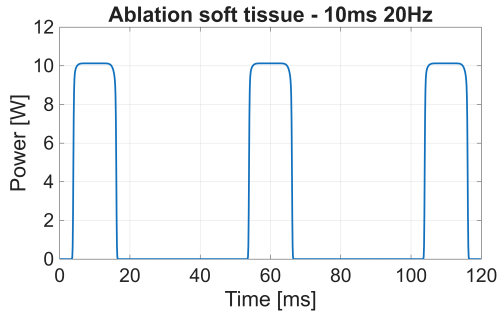


(c) Single pulse with pulse duration of 0.2 ms and repetition rate = 500 Hz

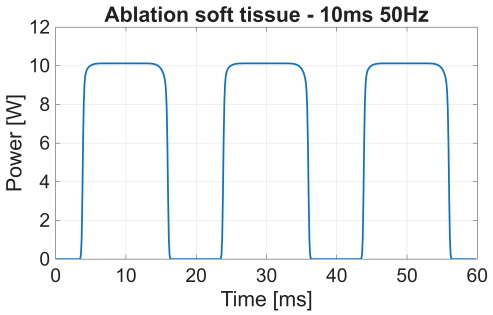
Figure 4.5: Amplification of a single pulse with different pulse durations and repetition rate.

Lastly, a simulation of the pulse train was performed in order to verify the correct temporal behavior of the amplifier. The values for pulse duration and repetition rate were taken from Tab. 4.1. Figures 4.6 to 4.8 show the simulated pulse trains for the three intended surgical applications: hemostasis, soft tissue ablation and kidney stone ablation respectively. In all cases the output pulse shape is well-defined and stable across successive pulses with a peak power of approximately 10 W which is consistent with the target specifications. The pulse train for hemostasis (Fig. 4.8) was simulated at a fixed repetition rate of 1 Hz with pulse durations of 100 ms, 250 ms and 500 ms. As the pulse duration increases the duty cycle grows accordingly, the

off-time gets lower and lower between consecutive pulses. The soft tissue ablation case (Fig. 4.6) uses a fixed pulse duration of 10 ms at repetition rates of 20 Hz and 50 Hz. The higher repetition rate results in a denser pulse train while preserving the individual pulse shape. Lastly, the kidney stone ablation case (Fig. 4.7) employs much shorter pulses of 0.05 ms at repetition rates of 10 Hz and 500 Hz. At 500 Hz the pulses become extremely dense and the peak power, visible in the zoomed part, remains consistent with the other operating regimes. In all simulated scenarios the amplifier responds correctly to the varying pulse parameters.

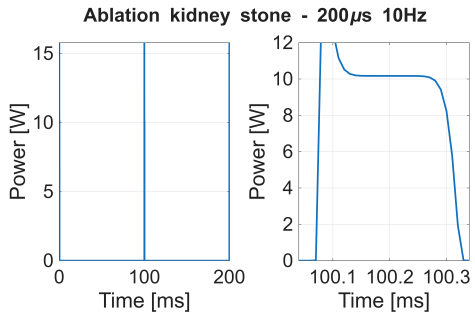


(a) Pulse train used for ablation of soft tissues, pulse duration = 10 ms and repetition rate = 20 Hz

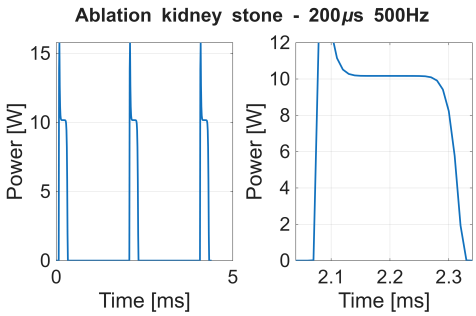


(b) Pulse train used for ablation of soft tissues, pulse duration = 10 ms and repetition rate = 50 Hz

Figure 4.6: Pulse train for soft tissue ablation.

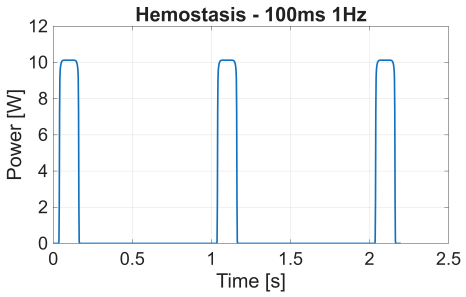


(a) Pulse train used for ablation of kidney stones, pulse duration = 0.2 ms and repetition rate = 10 Hz

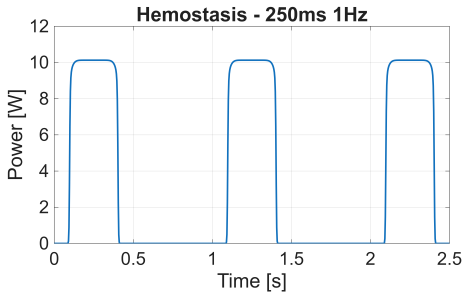


(b) Pulse train used for ablation of kidney stones, pulse duration = 0.2 ms and repetition rate = 500 Hz

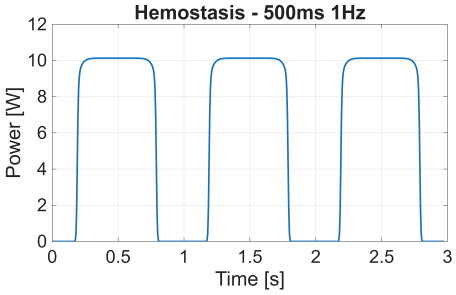
Figure 4.7: Pulse train for kidney stone ablation.



(a) Pulse train used for hemostasis, pulse duration of 100 ms and repetition rate = 1 Hz



(b) Pulse train used for hemostasis, pulse duration = 250 ms and repetition rate = 1 Hz



(c) Pulse train used for hemostasis, pulse duration = 500 ms and repetition rate = 1 Hz

Figure 4.8: Pulse train for hemostasis.

Tab. 4.4 contains a summary of the various combinations of pulse durations and repetition rates for the simulated pulses.

Table 4.4: Simulated pulses

Technique	**Pulse duration**	**Repetition rate**
Ablation (soft tissues)	10 ms	20 Hz
		50 Hz
Ablation (kidney stone)	0.2 ms	10 Hz
		500 Hz
Hemostasis	100 ms	1 Hz
	200 ms	
	500 ms	

4.3.2 Stimulated Brillouin Scattering

SBS is a nonlinear optical process that derives from the coupling between light and acoustic waves (phonons) propagating through a medium. SBS was theoretically predicted in 1922 and experimentally observed, for the first time, in 1964 inside

quartz and sapphire using an intense ruby MASER beam. The physical mechanism behind SBS is electrostriction, this phenomenon induces a periodic perturbation of the local material density generating an acoustic wave.

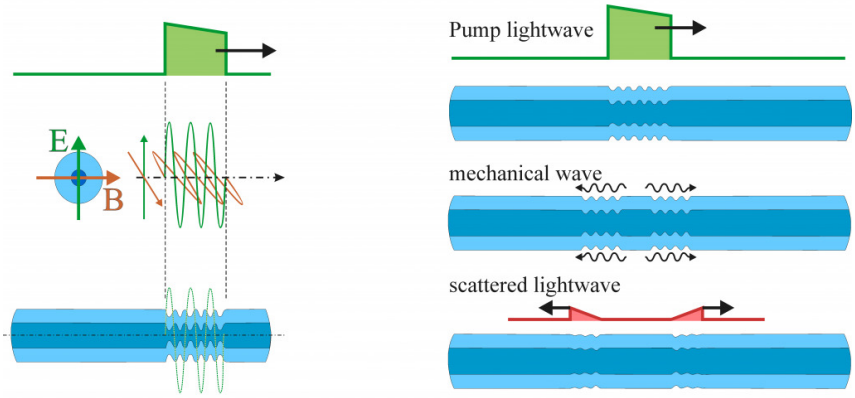


Figure 4.9: The traveling lightwave has both electrical field (E) and magnetic field (B) components (left), the lightwave (photons) interact with the vibrational states of the material (phonons) changing the photons energy and consequently their wavelength (right) [8].

The sound waves create a sort of modulation in the fiber refractive index which scatter the light in the backward and forward direction. Due the moving nature of the sound waves the scattered light is subject to the Doppler effect. The frequency downshift, derived from the Doppler effect, typically lies in the range of 10/11 GHz for standard silica optical fibers. The backscattered wave then interferes with the input pump wave and reinforces the acoustic grating through electrostriction, establishing a positive feedback loop. As a consequence, energy is efficiently transferred from the pump to the scattered light (Stokes wave). In optical fibers the SBS process is particularly significant because the guided geometry constrains the interaction to only two preferred propagation directions which are forward and backward. Since forward Brillouin scattering in optical fibers is negligible the Stokes wave propagates almost entirely in the direction opposite to the pump. A key parameter for characterizing SBS in fiber amplifiers is the SBS Threshold power (SBST) defined as the input pump power at which the backscattered Stokes power reaches a fixed fraction of the input power. Above threshold the Stokes power increases rapidly and may approach the pump power level. The SBST depends on the fiber length, the fiber loss coefficient, the Brillouin gain coefficient and the acousto-optic effective area (which describes the overlap integral between the optical and acoustic mode profiles). The Brillouin gain coefficient g_B depends on various material parameters including the square of the elasto-optic coefficient, the Brillouin linewidth, the density, the acoustic velocity and the refractive index (e.g. $g_B = 5 \cdot 10^{-11}$ m/W for silica). The Brillouin gain in decibels can be estimated as

$$G_B = 4.34\, g_B I_p L \tag{4.5}$$

where I_p is the spatially averaged intensity of the pump wave and L is the propagation length. It should be noted that this expression holds only under simplifying

assumptions and may not be valid for transient phenomena involving short light pulses. For standard single-mode fibers the SBST can be approximated as

$$P_{\text{th}} \approx \frac{21 A_{\text{eff}}}{g_B L_{\text{eff}}} \tag{4.6}$$

where A_{eff} is the optical effective area of the fiber and $L_{\text{eff}} = (1 - e^{-\alpha L})/\alpha$ is the effective interaction length, with α being the fiber loss coefficient and L the physical fiber length. In the context of high-power fiber amplifiers SBS represents a critical limiting factor. When the signal power exceeds the SBST a significant fraction of the optical energy is redirected into the backward-propagating wave rather than contributing to the amplified output directly reducing the achievable output power. Furthermore, the intense backward-propagating wave can damage upstream optical components, such as the pump laser or optical isolators, or the fiber itself as reported in Fig. 4.10. Moreover, the rapid energy transfer to the acoustic field generates localized heating within the fiber that may compromise its structural integrity. Lastly, in telecommunication context, the forward wave can deteriorate the bit error rate by adding noise to the amplification process. For these reasons SBS sets a practical upper bound on the output power of fiber amplifiers and must be carefully accounted for in the amplifier design. All the theory in this paragraph was retrieved from [44–47].

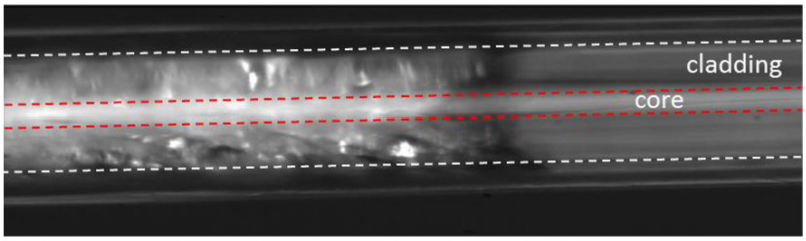


Figure 4.10: Example of SBS induced damages [4].

4.3.3 Simulated physical quantities for laser-tissue interaction and comparison with reference values

As explained in 4.1 pulse's energy and average power play a critical role during surgery as changing the given amount of energy delivered to the patient, as well as the average power, changes the effect of the treatment. For this reason once the simulations were completed a comparison between the theoretical values and the values found in the simulation was performed, the results are reported in Tab. 4.5.

With regard to the energy of the pulse the agreement between the values reported in the literature and those obtained from the simulations is evident. When observing the ablation of kidney stones, it can be seen that the pulse energy is slightly lower than the minimum value reported in the theoretical data. This is due to the chosen pulse duration: as explained before, only the lower part of the range was checked, since low pulse durations can trigger SBS. The upper values of the range were not checked, as other simulations were performed at those pulse durations, confirming that the system would have worked under those conditions as well. Both soft tissue

ablation and kidney stone ablation have the same energy, even though more than one simulation was performed, since the pulse duration is fixed while the repetition rate changes. The opposite situation is observed in the case of hemostasis where the repetition rate is fixed while the pulse duration changes. This behavior leads to a variable pulse energy which is proportional to the pulse duration.

Regarding the average power, Tab. 4.5 shows that all the adopted techniques have a minimum and maximum value of average power, this behavior can be explained by the fact that the average power depends on both the pulse energy and the repetition rate. Another thing that must be mentioned is that, although hemostasis and kidney stone ablation have almost the same average power range, the effects on the body are completely different. This difference is explained in 4.1, as the delivered power is the same but the pulse duration is completely different. A small Δt, as in the case of kidney stone ablation, means that the thermal confinement regime is the one applied to the body: the damage is localized and the heat cannot spread, allowing correct kidney stone ablation while avoiding heat damage to the kidney. On the other hand, a big Δt, as in the case of hemostasis, means that the photothermal regime is the one applied to the body: basically no damage is inflicted to the tissue while the heat spreads, allowing correct hemostasis.

Table 4.5: Pulse's energy for Ablation and Hemostasis, [10–13]

Technique	**Pulse energy (theory)**	**Pulse energy (simulated)**	**Average power (theory)**
Ablation (soft tissues)	100 mJ to 250 mJ	100 mJ	20 mW to 5 W
Ablation (kidney stone)	25 mJ to 6 J	20 mJ	2 W to 5 W
Hemostasis	1.5 J to 7.5 J	1 J to 5 J	1 W to 5 W

4.4 MATLAB simulations

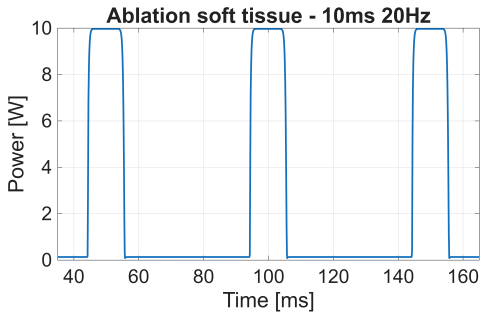
Due to the problems of the closed ecosystem of RP Fiber Power we wanted to find another way to perform the same simulations but using software that would offer greater flexibility and interoperability with other tools. For this reason, a MATLAB script was written and validated against the previously obtained results. To perform a meaningful comparison, the same pulse configurations were simulated according to the values reported in Tab. 4.4.

4.4.1 Optical simulations

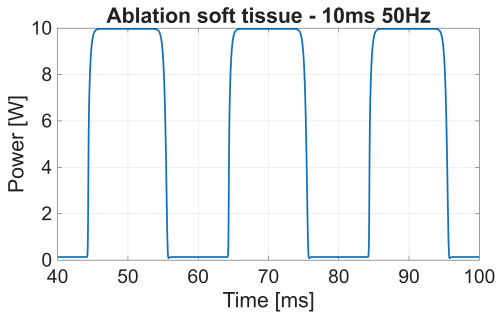
The results are organized according to the three intended clinical use cases: soft tissue ablation, kidney stone ablation and hemostasis. Fig. 4.11 reports the pulse trains for soft tissue ablation using a fixed pulse duration of 10 ms at repetition rates of 20 Hz and 50 Hz. At the higher repetition rate the pulses are more densely packed

in time but the individual pulse shape is preserved. Fig. 4.12 illustrates the kidney stone ablation regime which employs shorter pulses of 0.2 ms at repetition rates of 10 Hz and 500 Hz. At 500 Hz the pulse train becomes extremely dense, however the peak power and pulse shape remain consistent with the other operating regimes. The pulses are nearly identical across the two repetition rates, the only noticeable difference being a slight variation in the overshoot at the rising edge. Lastly, Fig. 4.13 shows the simulated pulse trains for hemostasis at a fixed repetition rate of 1 Hz with pulse durations of 100 ms, 250 ms and 500 ms. As expected, increasing the pulse duration raises the duty cycle and reduces the off-time between consecutive pulses while the overall shape remains well-defined.

Regarding pulse energy and average power what was said in the paragraph concerning the simulations performed in RP Fiber Power is still valid as the pulses shape, peak power and repetition rate are basically the same. The values reported in Tab. 4.5 can therefore be considered valid in this case as well.

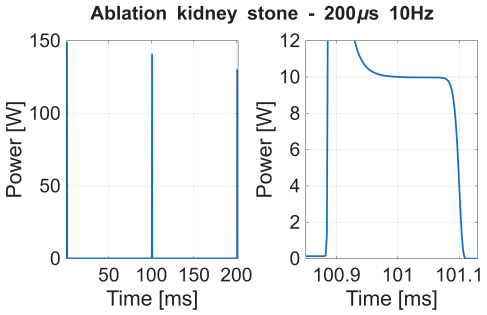


(a) Pulse train used for ablation of soft tissues, pulse duration = 10 ms and repetition rate = 20 Hz

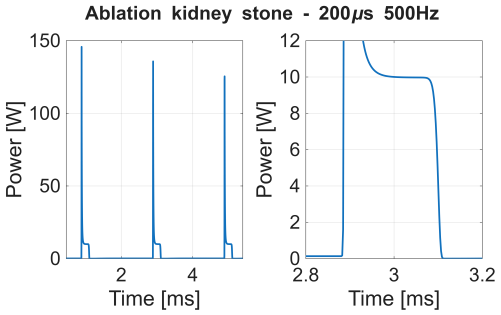


(b) Pulse train used for ablation of soft tissues, pulse duration = 10 ms and repetition rate = 50 Hz

Figure 4.11: Pulse train for soft tissue ablation.

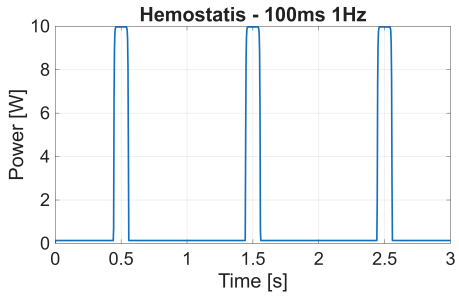


(a) Pulse train used for ablation of kidney stones, pulse duration = 0.2 ms and repetition rate = 10 Hz

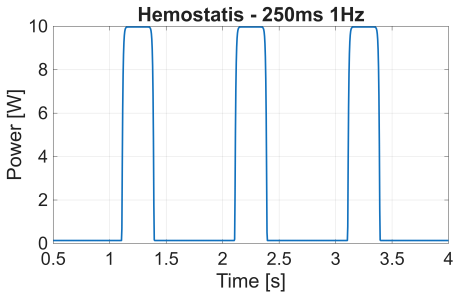


(b) Pulse train used for ablation of kidney stones, pulse duration = 0.2 ms and repetition rate = 500 Hz

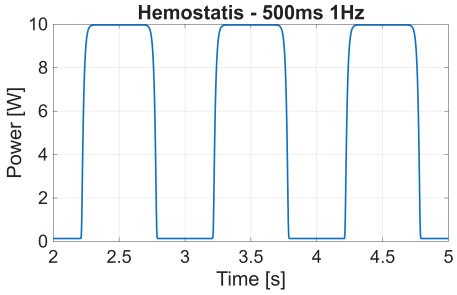
Figure 4.12: Pulse train for kidney stone ablation.



(a) Pulse train used for hemostasis, pulse duration of 100 ms and repetition rate = 1 Hz



(b) Pulse train used for hemostasis, pulse duration = 250 ms and repetition rate = 1 Hz



(c) Pulse train used for hemostasis, pulse duration = 500 ms and repetition rate = 1 Hz

Figure 4.13: Pulse train for hemostasis.

4.5 Comparison of the results of the two simulations

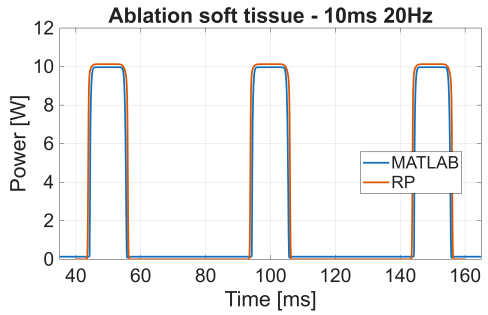
This section provides a comparative analysis of the results obtained from the two simulation models. To facilitate a direct comparison the results obtained from MATLAB and from RP Fiber Power have been superimposed. Since the two software environments adopt different temporal reference points for the pulse train origin a x-axis shift has been applied during post-processing in order to align the pulse trains and enable a meaningful side-by-side comparison. As a consequence, any apparent temporal discrepancies between the two waveforms should not be interpreted as physically meaningful differences but rather as artifacts introduced by this alignment procedure. Unless otherwise noted, all comparisons in the following analysis focus exclusively on pulse shape and amplitude.

Starting the analysis from the pulses for soft tissue ablation (Fig. 4.14) a good agreement between the softwares output can be observed. In both cases the MATLAB and RP traces overlap closely with peak power values reaching values in line with expectations. The pulse profile follows a super-Gaussian shape, as expected given the super-Gaussian nature of the input seed, indicating that the temporal envelope is preserved through the amplification stage. A slight difference in peak power between the two traces is visible in the plots, this discrepancy is small enough

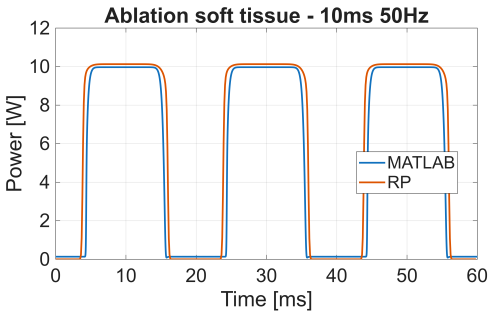
that can be neglected and the two waveforms can be considered identical. The pulse duration is also well maintained at 10 ms for both repetition rates tested (20 Hz and 50 Hz) confirming that the two models behave consistently regardless of the repetition rate.

The results obtained for the kidney stone ablation scenario (Fig. 4.15) show a good overall agreement between the two models, though some differences are more apparent than in the soft tissue case. The pulse shape is characterized by an initial overshoot followed by a gradual decay and both models reproduce this behavior consistently across the two repetition rates tested (10 Hz and 500 Hz). The pulse duration of 0.2 ms is well preserved in both cases. Looking more closely at the zoomed plots a discrepancy in the initial peak amplitude is visible. The MATLAB trace reaches a higher overshoot compared to the RP result while the subsequent decay profile matches reasonably well between the two. It is worth noting that the overshoot amplitude is not a fixed quantity: it can be adjusted by tuning the rise time of the leading edge of the input pulse, t_{rise}, allowing control over the peak power without altering the overall pulse energy or duration. The discrepancy between the MATLAB results and the RP ones can likely be attributed to the different discretization parameters used by the two simulators, rather than to a physical difference in the simulated system. Both system requires a given Δt and Δz which are the temporal step and the spatial step used to numerically integrate the propagation equations. For certain combinations of these two parameters, the computed overshoot can appear higher or lower. This does not represent a problem in itself, as the overshoot is a known physical feature correctly captured by both tools, the discrepancy is most likely due to the different discretization (combination of Δt and Δz) used in each simulation

The last case (hemostasis scenario, reported in Fig. 4.16) involves longer pulse durations at a fixed repetition rate of 1 Hz with three cases considered 100 ms, 250 ms and 500 ms. Across all three figures the MATLAB and RP Photonics models show very good agreement. Both traces overlap closely in terms of pulse shape, peak power and temporal width. The pulse profile is super-Gaussian in all cases, which is consistent with the input signal, and the peak power reaches approximately 10 W for both models throughout the entire pulse train. The pulse duration is well reproduced in each configuration with the flat-top region getting bigger and bigger starting from 100 ms to 500 ms as expected. Overall, the results confirm that the two models behave consistently across the full range of pulse durations considered validating the MATLAB implementation and its suitability for simulating pulse configurations relevant to this surgical context.

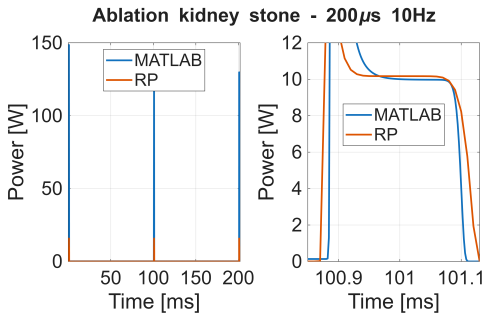


(a) Pulse train used for ablation of soft tissues, pulse duration = 10 ms and repetition rate = 20 Hz

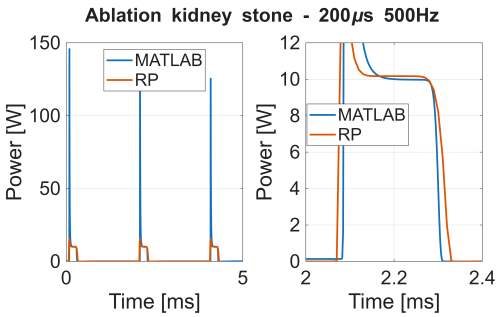


(b) Pulse train used for ablation of soft tissues, pulse duration = 10 ms and repetition rate = 50 Hz

Figure 4.14: Comparison between different pulse trains for soft tissue ablation.

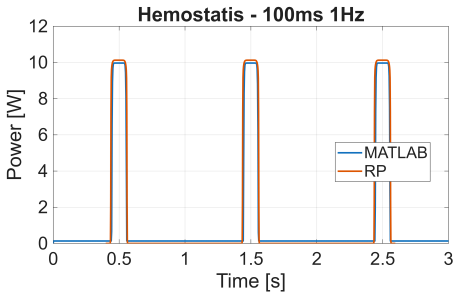


(a) Pulse train used for ablation of kidney stones, pulse duration = 0.2 ms and repetition rate = 10 Hz

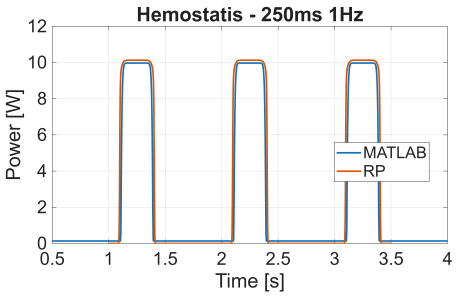


(b) Pulse train used for ablation of kidney stones, pulse duration = 0.2 ms and repetition rate = 500 Hz

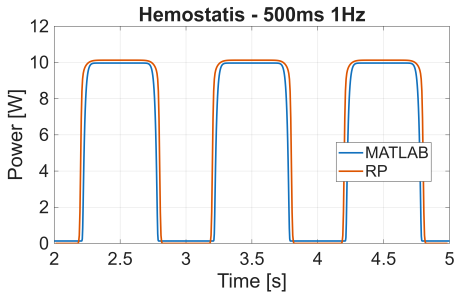
Figure 4.15: Comparison between different pulse trains for kidney stone ablation.



(a) Pulse train used for hemostasis, pulse duration of 100 ms and repetition rate = 1 Hz



(b) Pulse train used for hemostasis, pulse duration = 250 ms and repetition rate = 1 Hz



(c) Pulse train used for hemostasis, pulse duration = 500 ms and repetition rate = 1 Hz

Figure 4.16: Comparison between different pulse trains for hemostasis.

Chapter 5

Experimental evaluation

Due to procurement issues with the components needed to build the Thulium-based system described in the previous chapters it was decided to build a MOPA system using an Erbium/Ytterbium doped fiber instead. This different design allows us, at the cost of energy efficiency, to still reach the necessary pulses, but also to use the system as a basis for building a pump source for the Thulium system. The operation of this new system therefore remains the same as reported in the chapter explaining the MOPA theory and how light amplification occurs. The emission wavelength of this new system is 1550 nm. This wavelength is used not only in telecommunications but in this case it can also be used as a pump for a gain switched system based on TDFA. For this reason everything described below refers to the MOPA system with Erbium/Ytterbium fiber rather than the one originally planned in the theoretical section. Given the architectural equivalence of the two laser MOPA systems, the package dimensions and the power levels involved, all thermal simulations can be considered reliable.

5.1 Experimental setup

The experimental setup is shown by Fig. 5.1. The experimental setup consists of both optical components—including passive and active fibers, fiber splices, combiners, pump lasers, and a seed laser—and electronic instrumentation, such as bench power supplies, laser controllers, photodiodes, and an oscilloscope. The optical components are used to combine and amplify the seed signal, while the pump radiation excites the erbium and ytterbium ions in the active medium. The electronic instruments are employed to assess the system performance and acquire the data used to generate the plots presented in this thesis reported in Figures 5.3 to 5.5.

Regarding the optical part of the project, from Fig. 5.1 can be seen the pump laser (8) and seed laser (4). The seed is controlled by a LDC-3724 (2) which is a laser driver that allows the user to set a fixed operating current and temperature. In order to apply the pulse modulation reported in Tab. 4.4 to the seed laser an external function generator was used, this instrument is the Agilent 33220A (3). The pump laser, which requires a higher amount of power, is fixed to an external heatsink and powered by a Rigol DP832 bench power supply (10). To performed different test at different pump power the pump laser had to be driven through an

external control board. A National Instrument's board (9) was used in conjunction with PLD10K-CH driver board (7).

As briefly mentioned before, several different electronic instruments were used to perform all those measurements needed to asses if the system was properly functioning. Two different measurements had to be taken. In order to measure the signal power, the remaining pump and the sum of the two powers a power meter was used. An optical power meter is an instrument that measures the optical power (in W or dBm) of a laser beam or fiber-coupled signal, in this project a Thorlabs S442C (6) was implemented in the setup. On the other hand, a setup composed by a photodiode and an oscilloscope was implemented to asses the correct modulation of the output signal. Since this laser has to be used in a surgical context, a highly precise pulse train must be produced at the output to meet the required specifications. This setup was therefore needed to characterize the temporal evolution of the output power and to compare the results with the simulated pulses. The photodiode was a Thorlabs PDA10D2 (5) whereas the oscilloscope was a LeCroy WaveJet 354 (1).

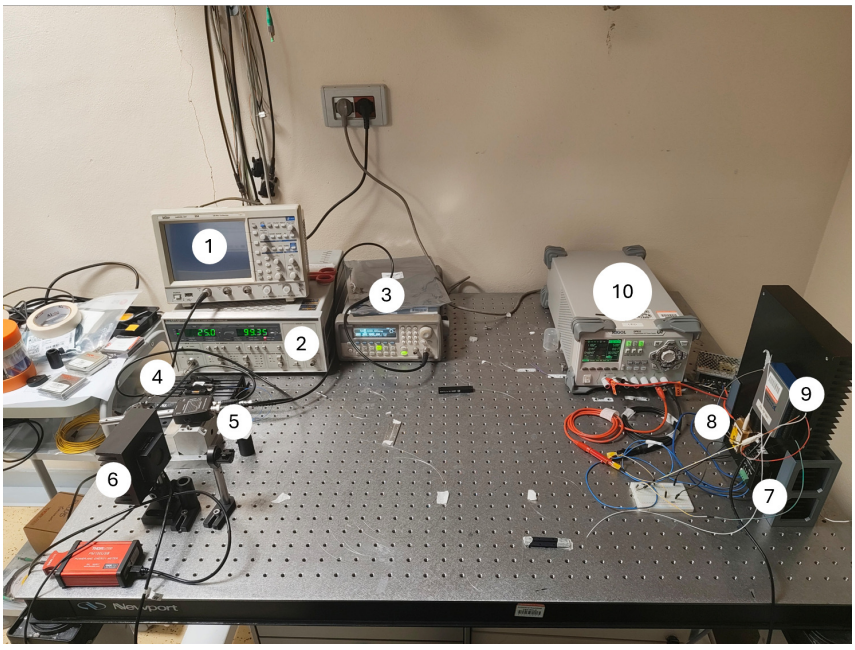


Figure 5.1: Experimental setup implemented MOPA laser.

5.1.1 Theory

Since the laser architecture is exactly the same of what was reported in the theory described in the first chapter Fig. 2.9 it can still be used as correct scheme for the setup. The only two differences are the seed and pump wavelength, now the seed laser emits at 1550 nm whereas the pump laser emits at 915 nm. What differs from the theory described before is the energy level system. What was reported by Fig. 2.7 cannot be applied for Erbium/Ytterbium, since pump absorption and signal emission occur on two different ion species rather than on a shared transition. For this reason an updated model is reported in Fig. 5.2.

Unlike the three-level Thulium system, described in Fig. 2.7, the Erbium/Ytterbium

co-doped system requires a more articulated energy level scheme. As shown in Fig. 5.2 the pump photons at 915 nm are absorbed by Yb^{3+} ions, promoting them from the ground state $^2F_{7/2}$ to the excited state $^2F_{5/2}$. The excitation energy is transferred non-radiatively from Yb^{3+} to neighboring Er^{3+} ions (transfer rate K), populating the $^4I_{11/2}$ level. From there, a fast relaxation (rate A_{MP}) brings the ion population down to the metastable $^4I_{13/2}$ level from which the 1550 nm signal is amplified via stimulated emission to the ground state $^4I_{15/2}$. At sufficiently high pump/signal intensities the up-conversion (rate C) between two ions in the $^4I_{13/2}$ level can promote one ion to the $^4I_{9/2}$ level rather than returning to the ground state, this behavior represents a parasitic loss mechanism that reduces the achievable gain. The Yb^{3+} and Er^{3+} metastable lifetimes are denoted τ_{Yb} and τ_{Er} respectively.

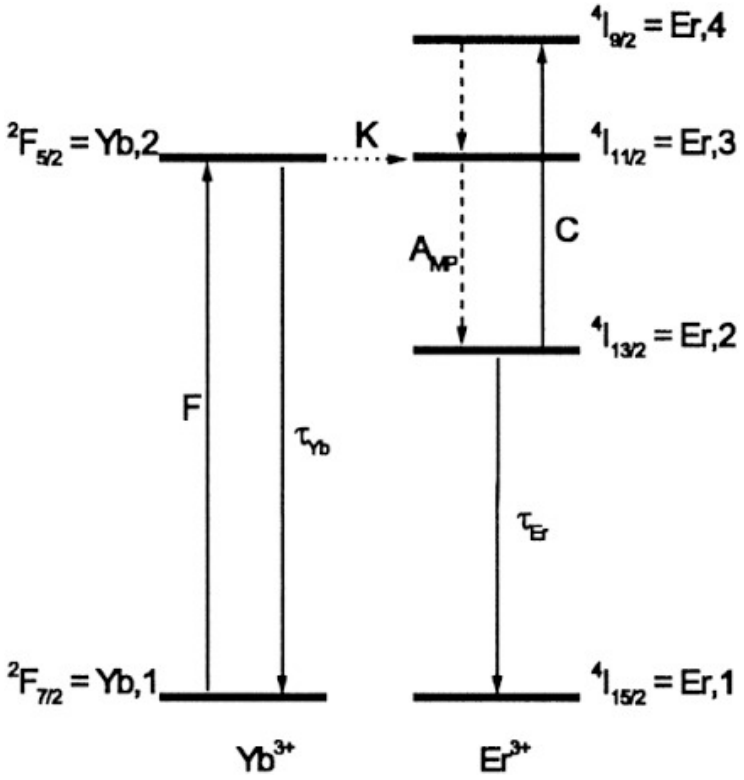


Figure 5.2: Diagram of co-doped Erbium/Ytterbium energy levels [9].

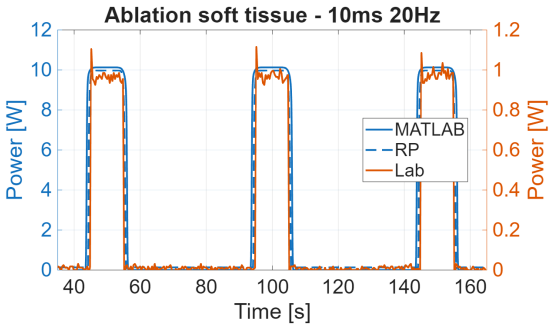
5.2 Experimental setup characterization

Two different characterizations were performed. The emitted power of the laser was measured to calculate the efficiency of the system. In order to do so three different measurement had to be taken: the first one is needed to evaluate the total emitted power, the second one aimed to evaluate the seed power at 1550 nm whereas the third was performed to check how much pump was present at the output. The total power can be considered as the sum of the seed power and the pump power. Ideally, the total power balance should consist entirely of the seed signal but, as the system consists in a real setup, this ideal case cannot be achieved. In this case the achieved efficiency was quite low, for this reason the amplification was not correctly performed by the system resulting in a weak seed signal at the output and high

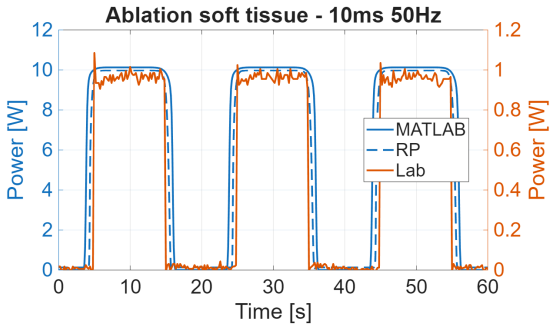
residual pump power. The average signal power is in the order of 200 mW while the pump's is 800 mW. The emitted total power is roughly 1 W.

5.2.1 Simulation vs. experimental measurements

By means of the oscilloscope, the temporal shape of the pulses was checked. The traces obtained from the oscilloscope can be seen in Figures 5.3 to 5.5. The shape of the pulses closely matches the simulated ones confirming that the temporal dynamics predicted by the models are consistent with the experimental behavior of the system. Since the peak power actually achieved on the bench was significantly lower than the one predicted by the simulations, a secondary y-axis with a different scale was used in Figures 5.3 to 5.5 to plot the experimental traces alongside the simulated ones. The comparison shown here therefore concerns the pulse shape, while the quantitative comparison in terms of energy is addressed in the next paragraph, where a scaling factor is introduced to account for this power gap. This agreement confirms that the programs used to simulate the system, both in MATLAB and in RP Fiber Power, were correctly modelled and can be used for further studies on this type of laser. The pulse peak power reached during the experimental characterization is approximately 1 W, the seed signal alone could not be measured separately because it was not possible to mount the filter between the photodiode connected to the oscilloscope and the fiber tip.

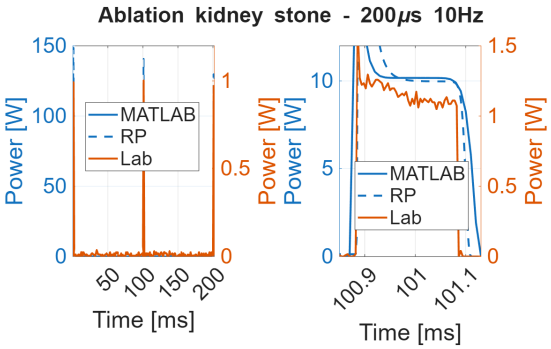


(a) Pulse train used for ablation of soft tissues, pulse duration = 10 ms and repetition rate = 20 Hz

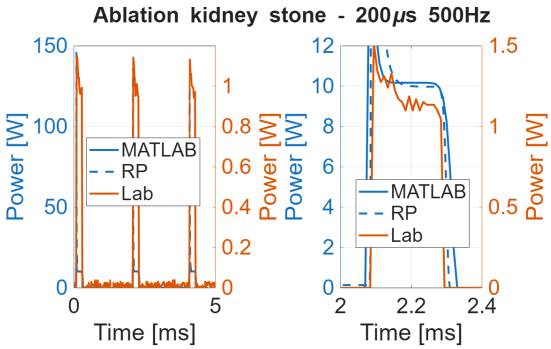


(b) Pulse train used for ablation of soft tissues, pulse duration = 10 ms and repetition rate = 50 Hz

Figure 5.3: Comparison between MATLAB and RP Fiber Power simulation with experimental data.

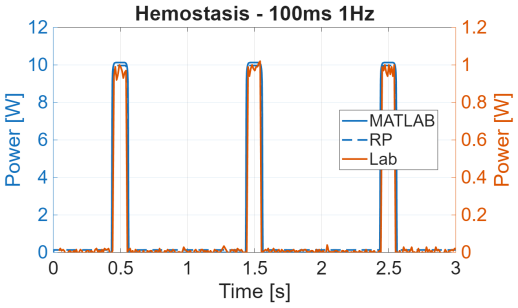


(a) Pulse train used for ablation of kidney stones, pulse duration = 0.2 ms and repetition rate = 10 Hz

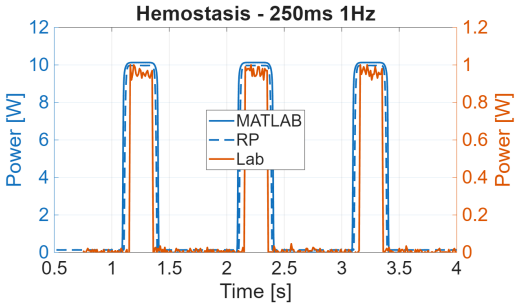


(b) Pulse train used for ablation of kidney stones, pulse duration = 0.2 ms and repetition rate = 500 Hz

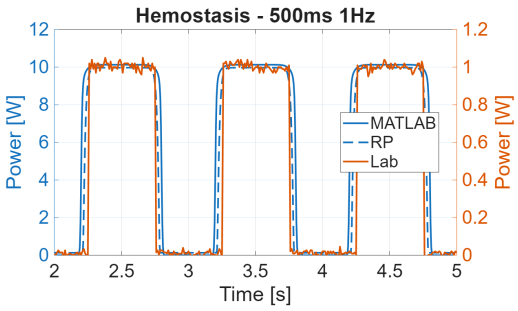
Figure 5.4: Comparison between MATLAB and RP Fiber Power simulation with experimental data.



(a) Pulse train used for hemostasis, pulse duration of 100 ms and repetition rate = 1 Hz



(b) Pulse train used for hemostasis, pulse duration = 250 ms and repetition rate = 1 Hz



(c) Pulse train used for hemostasis, pulse duration = 500 ms and repetition rate = 1 Hz

Figure 5.5: Comparison between MATLAB and RP Fiber Power simulation with experimental data.

5.2.2 Physical quantities relevant to laser-tissue interaction, comparison between: theory, simulation and experimental evaluation

Once the system behavior was characterized, the data were analyzed in order to perform a comparison between the theoretical, simulated and experimental data. This comparison is needed due to the necessity of assessing if the laser is able to provide the required energy for the various surgery techniques. As explained before, the average emitted power at the wanted wavelength is only a fraction of what it would have been, for this reason all the energy values of the experimental pulses were scaled up by a factor of $\frac{10\,\mathrm{W}}{0.2\,\mathrm{W}} = 50$ in order to perform a meaningful comparison. This scaling assumes that the pulse energy scales linearly with the average power meaning that repetition rate and pulse shape remain unchanged and that no additional saturation or thermal effects arise at higher power.

As displayed in Tab. 5.1, the pulse energy for soft tissue ablation is in close agreement with the simulated value and the hemostasis energy range (1.7 J to 3 J) falls within the simulated range (1 J to 5 J). The kidney stone ablation energy, on the other hand, is roughly one order of magnitude lower than the simulated value simulated. Since the same laser and emitted wavelength apply to all three techniques, this discrepancy cannot be attributed to setup or wavelength effects alone. The discrepancy of what was retrieved from literature and simulated could be imputed to the different setup and emitted wavelength that effect the overall laser efficiency.

Considering the hemostasis and soft tissue ablation energy values, the laser effectively works and can achieve the results discussed in the theoretical section for these two techniques. The kidney stone ablation case instead highlights a limitation of the current system and model, which should be addressed in future work. Despite this the model used both in MATLAB and RP Fiber Power have to be considered correct and they can be used for further simulations of similar systems.

Table 5.1: Pulse's energy for Ablation and Hemostasis. Comparison of the different values: theory, simulation and experimental evaluation

Technique	**Pulse energy (theory)**	**Pulse energy (simulated)**	**Pulse energy (experimental)**
Ablation (soft tissues)	100 mJ to 250 mJ	100 mJ	104.5 mJ
Ablation (kidney stone)	25 mJ to 6 J	20 mJ	1.7 mJ
Hemostasis	1.5 J to 7.5 J	1 J to 5 J	1.7 J to 3 J

5.2.3 Effect of pump power on signal characteristics

Since the amplification is directly correlated to the amount of pump power injected into the active fiber the behavior of the system under different pump powers was

checked. It is important to mention that the different pump powers are not reported in watts but rather in amperes, as those were the driving current values. Given that the pump module was driven at 12 V, the pump powers corresponding to the driving currents are respectively 9.6 W, 21.6 W and 33.6 W. The main objective was to assess whether the amplification scaled linearly with the pump power and, secondly, to check for the onset of saturation. The waveforms obtained at different pump powers are reported in Figures 5.6 to 5.8. Every graph shows that, for higher driving currents, the emitted power increases, which is consistent with the expected behavior. In addition to that, the shape of the pulse is correctly maintained across the different values of pump power. Looking at Fig. 5.7 it is evident that the pulse is not a clean square wave but rather shows an initial overshoot followed by a power droop whose magnitude decreases as the driving current increases. The other two pulses, Fig. 5.6 and Fig. 5.8, correctly resemble a square wave, which was the shape of the modulated pulse injected at the input of the fiber.

Looking at the reported graphs, it is evident that the output power does not scale linearly with the pump power. This phenomenon is particularly evident in Fig. 5.7 in which the increment from 1.8 A to 2.8 A is far smaller than the one from 0.8 A to 1.8 A. The same behavior can be also observed Fig. 5.8 even if, in this case, the magnitude of the saturation is lower than the previous reported case. The behavior of Fig. 5.7 can be explained by the fact that the pulse duration is very short compared to the gain dynamics of the active fiber, this operating regime does not allow the dopants inside the active fiber to absorb enough energy to invert the population to the level required to correctly amplify the signal. In the case of the other two pulses this behavior is reduced, if not completely absent, even if the pulse duration is considerably longer due to a considerably lower repetition rate. It is worth noting that Fig. 5.6 and Fig. 5.8 share approximately the same duty cycle, despite having repetition rates that differ by a factor of 20, and their output power values at each driving current are in close agreement with one another. This indicates that the observed threshold-like behavior does not depend on the duty cycle itself but rather on the repetition rate and the velocity of the TDFA to absorb the pump and invert the population.

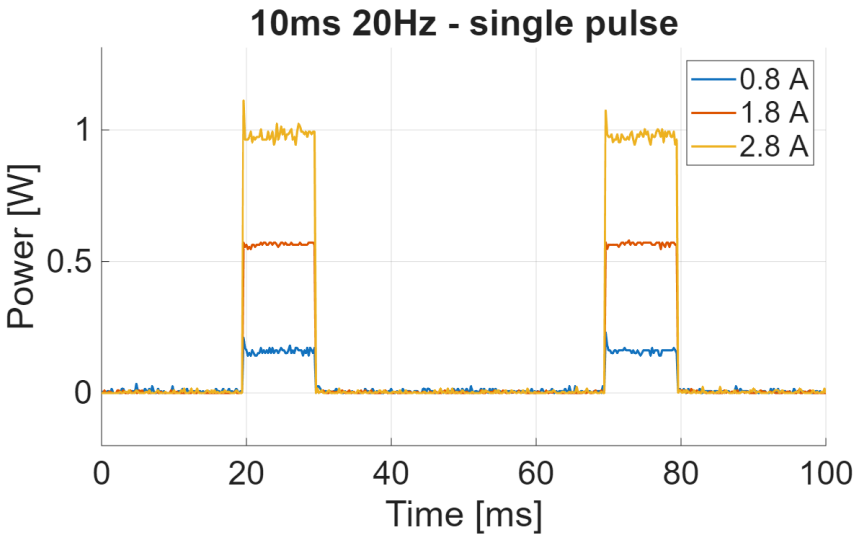


Figure 5.6: Superposition of pulses used for ablation of soft tissues at different pump power, pulse duration = 10 ms and repetition rate = 20 Hz.

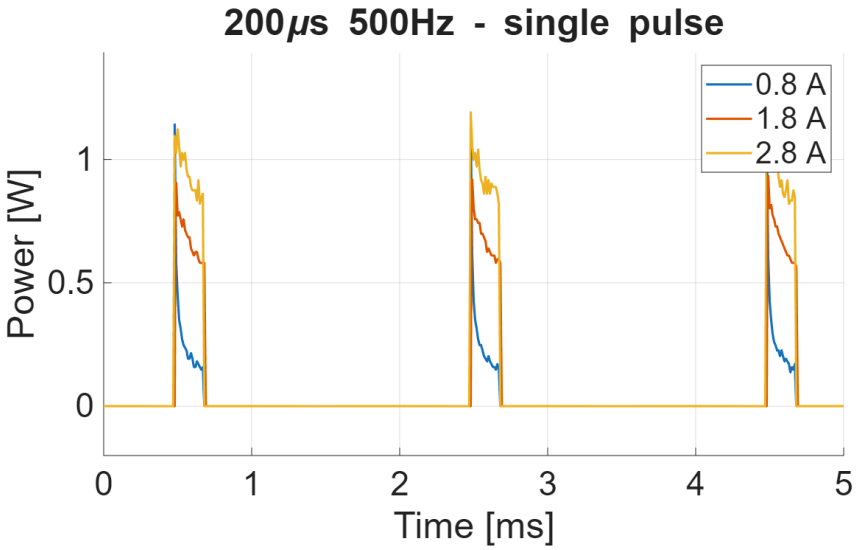


Figure 5.7: Superposition of pulses used for ablation of kidney stones at different pump power, pulse duration = 0.2 ms and repetition rate = 500 Hz.

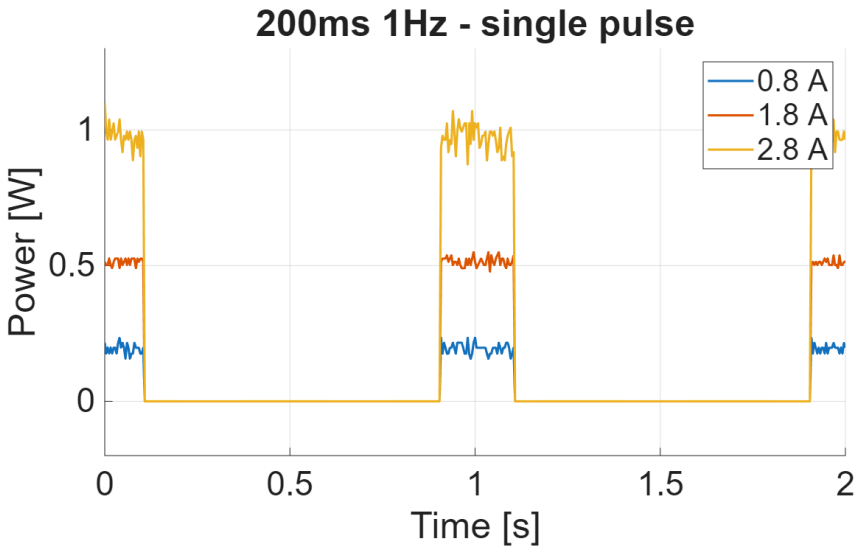


Figure 5.8: Superposition of pulses train used for hemostasis at different pump power, pulse duration = 200 ms and repetition rate = 1 Hz.

Chapter 6

Conclusion

The goal of this work was to build a laser system that can be used in a surgical environment to deliver minimally invasive surgeries. To achieve this result several simulations were performed, then the system was built and the results, obtained by experimental characterization, were confronted with what was simulated.

The thermal simulations showed that the model based on the CAD geometry was able to reproduce the thermal behavior of the real system with good accuracy. Moreover, the passive cooling solution proved to be effective, allowing the system to operate within acceptable temperature conditions even in the worst-case scenario Both the maximum temperature reached by the system and its dynamic thermal behavior were satisfactorily predicted by the simulations.

For the optical part, the simulations performed using both RP Fiber Power and MATLAB showed good agreement with the experimental data obtained in the laboratory. The measured pulse shapes were in good agreement with the simulated ones reproducing the expected temporal behavior for the different operating conditions. In particular, for pulse durations in the hundreds of microseconds, the overshoot observed in the simulations was also present in the oscilloscope traces, confirming that this feature was correctly reproduced by the models.

The experimental work implemented a MOPA architecture using a Erbium/Ytterbium active fiber due to the unavailability of the components needed for the Thulium version. This limitation prevented the direct experimental characterization of the simulated Thulium-based system. However, since the experimental setup shares the same MOPA architecture and comparable power levels, the results provide an experimental validation of the modelling approach and of the predicted system dynamics. The main difference between the simulated Thulium-based system and the experimental setup is the active fiber, resulting in a different operating wavelength. This difference is mainly related to the different experimental configuration, and therefore a direct quantitative comparison between the simulated target power and the experimental output power cannot be performed.

In conclusion, the results obtained in this work demonstrate the feasibility of the proposed approach. The thermal simulations showed that the passive cooling solu-

tion is sufficient to maintain the system within acceptable operating conditions and the comparison with experimental measurements confirmed the predicted thermal behavior. Similarly, the optical simulations performed with MATLAB and RP Fiber Power showed good agreement with the experimental pulse dynamics including the overshoot observed for short pulses. In the future some work could be done in order to implement and characterize the Thulium system with the optimization of its optical and thermal performance.

Bibliography

[1] J. Muncan and R. Tsenkova, "Aquaphotomics—From Innovative Knowledge to Integrative Platform in Science and Technology," *Molecules*, vol. 24, p. 2742, July 2019.

[2] https://ao-inc.com/products/optical-components/tosa/butterfly-package/, Mar. 2026.

[3] A. Rosiewicz and S. Coleman, "Development of a low SWaP laser transmitter," in *SPIE Optical Engineering + Applications* (E. W. Taylor and D. A. Cardimona, eds.), (San Diego, CA), p. 746703, Aug. 2009.

[4] M. N. Zervas and C. A. Codemard, "High Power Fiber Lasers: A Review," *IEEE Journal of Selected Topics in Quantum Electronics*, vol. 20, pp. 219–241, Sept. 2014.

[5] T. Maitiniyazi, "Power Scaling of Single-Mode Ytterbium and Erbium High-Power Fiber Lasers,"

[6] L. Piccolo, K. Bornillo, S. Micheli, M. Sorgato, M. Ricotta, E. Cimetta, and G. Lucchetta, "A penetration efficiency model for the optimization of solid conical microneedles' geometry," *Journal of Micromechanics and Microengineering*, vol. 34, p. 025009, Feb. 2024.

[7] D. Creeden, B. R. Johnson, G. A. Rines, and S. D. Setzler, "High power resonant pumping of Tm-doped fiber amplifiers in core- and cladding-pumped configurations," *Optics Express*, vol. 22, p. 29067, Nov. 2014.

[8] "Brillouin scattering." https://www.pulse-h2020.eu/brillouin-scattering/, Aug. 2026.

[9] J. Philipps, T. Töpfer, H. Ebendorff-Heidepriem, D. Ehrt, and R. Sauerbrey, "Energy transfer and upconversion in erbium–ytterbium-doped fluoride phosphate glasses," *Applied Physics B*, vol. 74, pp. 233–236, Mar. 2002.

[10] N. M. Fried and K. E. Murray, "High-Power Thulium Fiber Laser Ablation of Urinary Tissues at 1.94 µm," *Journal of Endourology*, vol. 19, pp. 25–31, Jan. 2005.

[11] O. Traxer and E. X. Keller, "Thulium fiber laser: The new player for kidney stone treatment? A comparison with Holmium:YAG laser," *World Journal of Urology*, vol. 38, pp. 1883–1894, Aug. 2020.

[12] A. Hutfilz, D. Theisen-Kunde, M. M. Bonsanto, and R. Brinkmann, "Pulsed thulium laser blood vessel haemostasis as an alternative to bipolar forceps during neurosurgical tumour resection," *Lasers in Medical Science*, vol. 38, p. 94, Mar. 2023.

[13] A. Vogel and V. Venugopalan, "Mechanisms of Pulsed Laser Ablation of Biological Tissues," *Chemical Reviews*, vol. 103, pp. 577–644, Feb. 2003.

[14] J. P. Gordon, H. J. Zeiger, and C. H. Townes, "The Maser—New Type of Microwave Amplifier, Frequency Standard, and Spectrometer," *Physical Review*, vol. 99, pp. 1264–1274, Aug. 1955.

[15] A. L. Schawlow and C. H. Townes, "Infrared and Optical Masers," *Physical Review*, vol. 112, pp. 1940–1949, Dec. 1958.

[16] A. Javan, W. R. Bennett, and D. R. Herriott, "Population Inversion and Continuous Optical Maser Oscillation in a Gas Discharge Containing a He-Ne Mixture," *Physical Review Letters*, vol. 6, pp. 106–110, Feb. 1961.

[17] R. N. Hall, G. E. Fenner, J. D. Kingsley, T. J. Soltys, and R. O. Carlson, "Coherent Light Emission From GaAs Junctions," *Physical Review Letters*, vol. 9, pp. 366–368, Nov. 1962.

[18] H. Kroemer, "A proposed class of hetero-junction injection lasers," *Proceedings of the IEEE*, vol. 51, pp. 1782–1783, Dec. 1963.

[19] Z. I. Alferov, "Nobel Lecture: The double heterostructure concept and its applications in physics, electronics, and technology," *Reviews of Modern Physics*, vol. 73, pp. 767–782, Oct. 2001.

[20] E. Desurvire, J. R. Simpson, and P. C. Becker, "High-gain erbium-doped traveling-wave fiber amplifier,"

[21] D. J. Richardson, J. Nilsson, and W. A. Clarkson, "High power fiber lasers: Current status and future perspectives [Invited]," *Journal of the Optical Society of America B*, vol. 27, p. B63, Nov. 2010.

[22] K. Iizuka, *Elements of Photonics, Volume I*, vol. 1 of *Wiley Series in Pure and Applied Optics*. New York, USA: John Wiley & Sons, Inc., May 2002.

[23] W. Zeller, L. Naehle, P. Fuchs, F. Gerschuetz, L. Hildebrandt, and J. Koeth, "DFB Lasers Between 760 nm and 16 µm for Sensing Applications," *Sensors*, vol. 10, pp. 2492–2510, Mar. 2010.

[24] K. Iizuka, *Elements of Photonics*. New York, N.Y: Wiley-Interscience, 2002.

[25] W. Liu, P. Ma, H. Lv, J. Xu, P. Zhou, and Z. Jiang, "General analysis of SRS-limited high-power fiber lasers and design strategy," *Optics Express*, vol. 24, p. 26715, Nov. 2016.

[26] https://www.rp-photonics.com/master_oscillator_fiber_amplifier.html, Apr. 2026.

[27] P. Kaczmarek, G. Soboń, J. Sotor, A. Antończak, and K. Abramski, "Fiber-MOPA sources of coherent radiation," *Bulletin of the Polish Academy of Sciences: Technical Sciences*, vol. 58, Jan. 2010.

[28] J. Mirza, U. A. Salaria, S. Ghafoor, A. Atieh, B. Kanwal, A. Almogren, and I. Aziz, "Modeling and analysis of single-mode widely tunable all-fiber Ho-doped CW master oscillator power amplifier system," *Physica Scripta*, vol. 99, p. 085512, Aug. 2024.

[29] B. Dutta Gupta, S. Tang, T. Berthelot, S. Cozic, S. Poulain, and C. Aguergaray, "Towards high-power MOPA architectures in single-mode fibers for mid-IR mode-locked operation," *Optics Express*, vol. 32, p. 23448, June 2024.

[30] D. N. Schimpf, C. Ruchert, D. Nodop, J. Limpert, A. Tünnermann, and F. Salin, "Compensation of pulse-shaping due to saturation in fiber amplifiers," in *SPIE LASE: Lasers and Applications in Science and Engineering* (D. V. Gapontsev, D. A. Kliner, J. W. Dawson, and K. Tankala, eds.), (San Jose, CA), p. 71951E, Feb. 2009.

[31] L. Jin and Y. Liang, "Fiber laser technologies for photoacoustic microscopy," *Visual Computing for Industry, Biomedicine, and Art*, vol. 4, p. 11, Dec. 2021.

[32] M. Stephen, A. W. Yu, J. W. Nicholson, A. Hariharan, J. R. Chen, K. Numata, S. Wu, B. Gonzales, M. E. Fahey, M. Rodriguez, B. R. Bean, L. Han, M. E. Plants, G. Allan, W. Mamakos, and J. Abshire, "Fiber-based laser MOPA transmitter packaging for space environment," in *Components and Packaging for Laser Systems IV* (A. L. Glebov and P. O. Leisher, eds.), (San Francisco, United States), p. 7, SPIE, Feb. 2018.

[33] C. Kong, C. Pilger, H. Hachmeister, X. Wei, T. H. Cheung, C. S. W. Lai, T. Huser, Kevin. K. Tsia, and K. K. Y. Wong, "Compact fs ytterbium fiber laser at 1010 nm for biomedical applications," *Biomedical Optics Express*, vol. 8, p. 4921, Nov. 2017.

[34] A. T. Gursel, "Fiber Lasers and Their Medical Applications," in *Optical Amplifiers - A Few Different Dimensions* (P. K. Choudhury, ed.), InTech, July 2018.

[35] M. N. Zervas, "High power ytterbium-doped fiber lasers — fundamentals and applications," *International Journal of Modern Physics B*, vol. 28, p. 1442009, May 2014.

[36] X. Shu-Jie, "Two-micron (thulium) laser resection of the prostate-tangerine technique: A new method for BPH treatment," *Asian Journal of Andrology*, vol. 11, pp. 277–281, May 2009.

[37] G. Kurmuş, A. Tatlıparmak, B. Aksoy, E. Koç, Z. Aşiran Serdar, and C. Ergin, "Efficacy and safety of 1927 nm fractional Thulium fiber laser for the treatment of melasma: A retrospective study of 100 patients," *Journal of Cosmetic and Laser Therapy*, vol. 21, pp. 408–411, Nov. 2019.

[38] W.-Y. Xu, G. Wang, Y.-F. Li, Y. Yu, Y. Wang, and Z. Lu, "Frontier Advances and Challenges of High-Power Thulium-Doped Fiber Lasers in Minimally Invasive Medicine," *Photonics*, vol. 12, p. 614, June 2025.

[39] M. Schembri, J. Sahu, O. Aboumarzouk, A. Pietropaolo, and B. K. Somani, "Thulium fiber laser: The new kid on the block," *Urology Research and Practice*, vol. 46, pp. S1–S10, May 2020.

[40] A. N. Bashkatov, E. A. Genina, V. I. Kochubey, and V. V. Tuchin, "Optical properties of human skin, subcutaneous and mucous tissues in the wavelength range from 400 to 2000 nm," *Journal of Physics D: Applied Physics*, vol. 38, pp. 2543–2555, Aug. 2005.

[41] P. D. McGovern, M. Albrecht, K. G. Belani, C. Nachtsheim, P. F. Partington, I. Carluke, and M. R. Reed, "Forced-air warming and ultra-clean ventilation do not mix: An investigation of theatre ventilation, patient warming and joint replacement infection in orthopaedics," *The Journal of Bone and Joint Surgery. British volume*, vol. 93-B, pp. 1537–1544, Nov. 2011.

[42] M. Albrecht, R. Gauthier, and D. Leaper, "Forced-air warming: A source of airborne contamination in the operating room?," *Orthopedic Review*, vol. 1, Oct. 2009.

[43] C. Li, Y. Fan, W. Li, K. Yuan, T. Fu, J. Liu, C.-e. Zah, and C. He, "High power conductively cooled laser diode array operating under hard pulse condition," in *Components and Packaging for Laser Systems VIII* (A. L. Glebov and P. O. Leisher, eds.), (San Francisco, United States), p. 2, SPIE, Mar. 2022.

[44] R. Paschotta, "Brillouin scattering." RP Photonics Encyclopedia, 2021.

[45] A. Kobyakov, M. Sauer, and D. Chowdhury, "Stimulated Brillouin scattering in optical fibers," *Advances in Optics and Photonics*, vol. 2, p. 1, Mar. 2010.

[46] R. Y. Chiao, C. H. Townes, and B. P. Stoicheff, "Stimulated Brillouin Scattering and Coherent Generation of Intense Hypersonic Waves," *Physical Review Letters*, vol. 12, pp. 592–595, May 1964.

[47] B. J. Eggleton, C. G. Poulton, P. T. Rakich, Michael. J. Steel, and G. Bahl, "Brillouin integrated photonics," *Nature Photonics*, vol. 13, pp. 664–677, Oct. 2019.